Beijing Climate Center Earth System Model version 1 (BCC-ESM1): Model Description and Evaluation of Aerosol Simulations

Tongwen Wu[1*], Fang Zhang[1], Jie Zhang[1], Weihua Jie[1], Yanwu Zhang[1], Fanghua Wu[1], Laurent Li[1,2], Jinghui Yan[1], Xiaohong Liu[3], Xiao Lu[4], Haiyue Tan[4], Lin Zhang[4], Jun Wang[5], Aixue Hu[6]

[1]Beijing Climate Center, China Meteorological Administration, Beijing, China

[2]Laboratoire de Météorologie Dynamique, IPSL, CNRS, Sorbonne Université, Ecole Normale Supérieure, Ecole Polytechnique, Paris, France

[3] Texas A&M University, College Station, TX, USA

[4] Laboratory for Climate and Ocean-Atmosphere Studies, Department of Atmospheric and Oceanic Sciences, School of Physics, Peking University, Beijing, China

[5] University of Iowa, Iowa City, IA 52242, USA

[6]National Center for Atmospheric Research, PO Box 3000, Boulder, Colorado 80307-3000, USA

Correspondence to: Tongwen Wu (twwu@cma.gov.cn)

Submit to Geosci. Model Dev.

Revised on Oct. 23, 2019

Revised on Dec. 14, 2019

Revised on Jan. 17, 2020

Abstract. BCC-ESM1 is the first version of a fully-coupled Earth System Model with interactive atmospheric chemistry and aerosols developed by the Beijing Climate Center, China Meteorological Administration. Major aerosol species (including sulfate, organic carbon, black carbon, dust and sea salt) and greenhouse gases are interactively simulated with a whole panoply of processes controlling emission, transport, gas-phase chemical reactions, secondary aerosol formation, gravitational settling, dry deposition, and wet scavenging by clouds and precipitation. Effects of aerosols on radiation, cloud, and precipitation are fully treated. The performance of BCC-ESM1 in simulating aerosols and their optical properties is comprehensively evaluated as required by the Aerosol Chemistry Model Intercomparison Project (AerChemMIP), covering the preindustrial mean state and time evolution from 1850 to 2014. The simulated aerosols from BCC-ESM1 are quite coherent with CMIP5-recommended data, in-situ measurements from surface networks (such as IMPROVE in the U.S. and EMEP in Europe), and aircraft observations. A comparison of modeled aerosol optical depth (AOD) at 550 nm with satellite observations retrieved from Moderate Resolution Imaging Spectroradiometer (MODIS) and Multi-angle Imaging SpectroRadiometer (MISR) and surface AOD observations from AErosol RObotic NETwork (AERONET) shows reasonable agreements between simulated and observed AOD. However, BCC-ESM1 shows weaker upward transport of aerosols from the surface to the middle and upper troposphere, likely reflecting the deficiency of representing deep convective transport of chemical species in BCC-ESM1. With an overall good agreement between BCC-ESM1 simulated and observed aerosol properties, it demonstrates a success of the implementation of interactive aerosol and atmospheric chemistry in BCC-ESM1.

1. Introduction

Atmosphere is a thin gaseous layer around the Earth, consisting of nitrogen, oxygen and a large number of trace gases including important greenhouse gases (GHG) such as water vapor, tropospheric ozone (O_3), carbon dioxide (CO_2), methane (CH_4), nitrous oxide (N_2O), and chloro-fluoro-carbons (CFCs). Besides gaseous components, atmosphere also contains various aerosols, which are important for cloud formation and radiative transfer. Atmospheric trace gases and aerosols are actually interactive components of the climate system. Their inclusion in global climate models (GCMs) is a significant enhancement for most state-of-the-art climate models (Lamarque et al., 2013; Collins et al., 2017). Early attempts in coupling global climate dynamics with atmospheric chemistry can be traced back to late 1970s, when 3D transport of ozone and simple stratospheric chemistry were firstly incorporated into a GCM to simulate global O_3 production and transport (e.g., Cunnold et al. 1975; Schlesinger and Mintz 1979). Since mid-1980s, a large number of on-line global climate/chemistry models have been developed to address issues of the Antarctic stratospheric O_3 depletion (e.g., Cariolle et al. 1990; Austin et al. 1992; Solomon, 1999), tropospheric O_3 and sulfur cycle (e.g., Feichter et al. 1996; Barth et al. 2000), tropospheric aerosol and its interactions with cloud (e.g., Chuang et al. 1997; Lohmann et al. 2000; Ghan and Easter, 2006; Jacobson 2012). Aerosols and chemically reactive gases in the atmosphere exert important influences on global and regional air quality and climate (Collins et al., 2017).

Since 2013, the Beijing Climate Center (BCC), China Meteorological Administration, has continuously developed and updated its fully-coupled GCM, the Beijing Climate Center Climate System Model (BCC-CSM) (Wu et al., 2013; Wu et al., 2014; Wu et al., 2019). BCC-CSM version 1.1 was one of the comprehensive carbon-climate models participating in the phase five of the Coupled Model Intercomparison Project (CMIP5, Taylor et al. 2012). When forced by prescribed historical emissions of CO_2 from combustion of fossil fuels and land use change, BCC-CSM1.1 successfully reproduced the trends of observed atmospheric CO_2 concentration and global surface air temperature from 1850 to 2005 (Wu et al., 2013). During recent years, BCC-CSM1.1 has been used in numerous investigations on soil organic carbon changes (e.g. Todd-Brown et al., 2014), ocean biogeochemistry changes (e.g. Mora et al., 2013), and carbon-climate feedbacks (e.g. Arora et al., 2013; Hoffman et al., 2014).

81 BCC-CSM includes main climate-carbon cycle processes (Wu et al., 2013) and the global

82 mean atmospheric CO_2 concentration is calculated from a prognostic equation of CO_2 budget

83 taking into account global anthropogenic CO_2 emissions and interactive land-atmosphere and

84 ocean-atmosphere CO2 exchanges.

85 In recent years, BCC has put large efforts in developing a global

86 climate-chemistry-aerosol fully-coupled Earth System Model (BCC-ESM1) on the basis of

87 BCC-CSM2 (Wu et al., 2019). The objective is to interactively simulate global aerosols (e.g.

88 sulfate, black carbon, etc.) and main greenhouse gases (e.g. O_3, CH_4, N_2O and CO_2) in the

89 atmosphere and to investigate feedbacks between climate and atmospheric chemistry.

90 BCC-ESM1 is at the point to be publicly released, and it is actively used by BCC for several

91 CMIP6-endorsed research initiatives (Eyring et al. 2016), including the Aerosol Chemistry

92 Model Intercomparison Project (AerChemMIP, Collins et al., 2017) and the Coupled

93 Climate–Carbon Cycle Model Intercomparison Project (C4MIP, Jones et al. 2016).

94 The purpose of this paper is to evaluate the performance of BCC-ESM1 in simulating

95 aerosols and their optical properties in the 20th century. The description of BCC-ESM1 is

96 presented in Section 2. The experimental protocol is given in Section 3. Section 4 presents the

97 evaluations of aerosol simulations with comparisons to CMIP5-recommended data (Lamarque

98 et al., 2010) and data obtained from both global surface networks and satellite observations.

99 The regional and global characteristics compared to observations and estimates from other

100 studies are analyzed. Simulations of aerosol optical properties in the 20th century are also

101 analyzed in Section 4. Conclusions and discussions are summarized in Section 5. Information

102 about code and data availability is given in Section 6.

103 **2. Model description**

104 BCC-ESM1 is an Earth System Model with interactive chemistry and aerosol

105 components, in which the atmospheric component is BCC Atmospheric General Model

106 version 3 (Wu et al., 2019) with interactive atmospheric chemistry (hereafter

107 BCC-AGCM3-Chem), land component BCC Atmosphere and Vegetation Interaction Model

108 version 2.0 (hereafter BCC-AVIM2.0), ocean component Modular Ocean Model version 4

109 (MOM4)-L40, and sea ice component [sea ice simulator (SIS)]. Different components of

110 BCC-ESM1 are fully coupled and interact with each other through fluxes of momentum,

energy, water, carbon and other tracers at their interfaces. The coupling between the atmosphere and the ocean is done every hour.

The atmospheric component BCC-AGCM3-Chem is able to simulate global atmospheric composition and aerosols from anthropogenic emissions as forcing agents. Its resolution is T42 (approximately 2.8125 °×2.8125 ° transformed spectral grid). The model has 26 levels in a hybrid sigma/pressure vertical coordinate system with the top level at 2.914 hPa. Details of the model physics are described in Wu et al. (2019). The BCC-AGCM3-Chem combines 66 gas-phase chemical species and 13 bulk aerosol compounds as listed in Table 1. Apart from 3 gas-phase species of dimethyl sulfide (DMS), sulfur dioxide (SO_2) and ammonia (NH_3), the other 63 gas-phase species are the same as those in the "standard version" of MOZART2 (Model for Ozone and Related chemical Tracers, version 2), a global chemical transport model for the troposphere developed by the National Center for Atmospheric Research (NCAR) driven by meteorological fields from either climate models or assimilations of meteorological observations (Horowitz et al., 2003). Advection of all tracers in BCC-AGCM3-Chem is performed through a semi-Lagrangian scheme (Williamson and Rasch, 1989), and vertical diffusion within the boundary layer follows the parameterization of Holtslag and Boville (1993). The gas-phase chemistry of the 63 MOZART2 gas-phase species as listed in Table 1 is treated in the same way as that in the "standard version" of MOZART2 (Horowitz et al., 2003), and there are 33 photolytic reactions and 135 chemical reactions involving 30 dry deposited chemical species and 25 soluble gas-phase species. Dry deposition velocities for the 15 trace gases including O_3, carbon monoxide (CO), CH_4, formaldehyde (CH_2O), acetic acid (CH_3OOH), hydrogen peroxide (H_2O_2), nitrogen dioxide (NO_2), nitric acid (HNO_3), polyacrylonitrile (PAN), acetone (CH_3COCH_3), peroxyacetic acid (CH_3COOOH), acetaldehyde (CH_3CHO), methylglyoxal (CH_3COCHO), nitric oxid (NO), and pernitric acid (HNO_4) are not computed interactively and directly interpolated from MOZART2 climatological monthly mean deposition velocities (https://en.wikipedia.org/wiki/MOZART(model)) which are calculated offline (Bey et al., 2001; Shindell et al., 2008) using a resistance-in-series scheme originally described in Wesely (1989). The dry deposition velocities for the other 15 species including peroxy acetyl nitrate (PAN), methyl nitroacetate (ONIT), organic nitrates (ONITR), ethyl alcohol (C_2H_5OH), organic

141 hydroxiperoxide (POOH), ethyl hydroperoxide (C_2H_5OOH), propylhydroperoxide

142 (C_3H_7OOH), methylene glycol mono acetate (ROOH), glycolaldehyde (GLYALD), acetol

143 (HYAC), methanol (CH_3OH), propanoic acid (MACROOH), isoprene hydroxy hydroperoxide

144 (ISOPOOH), carboxylic acid (XOOH), formaldehyde (HYDRALD), and hydrogen (H_2) are

145 calculated using prescribed deposition velocities of O_3, CO, CH_3CHO, or land surface type

146 and surface temperature following the MOZART2 (Horowitz et al., 2003). Wet removal by

147 in-cloud scavenging for 25 soluble gas-phase species in the "standard version" of MOZART2

148 uses the parameterization of Giorgi and Chameides (1985) based on their temperature

149 dependent effective Henry's law constants. In-cloud scavenging is proportional to the amount

150 of cloud condensate converted to precipitation, and the loss rate depends on the amount of

151 cloud water, the rate of precipitation formation, and the rate of tracer uptake by the liquid

152 phase water. Other highly soluble species such as HNO_3, H_2O_2, ONIT, ISOPOOH,

153 MACROOH, XOOH, and lead (Pb-210) are also removed by below-cloud washout as

154 calculated using the formulation of Brasseur et al. (1998). Below-cloud scavenging is

155 proportional to the precipitation flux in each model layer and the loss rate depends on the

156 precipitation rate. Vertical transport of gas tracers and aerosols due to deep convection is not

157 yet included in the present version of BCC-AGCM3-Chem, which process is considered as a

158 part of the deep convection and occurs generally in a small spatial region on a GCM-box with

159 low-resolution (2.8 ˚lat.×2.8 ˚lon.). Another consideration is that a large uncertainty exists to

160 treat transport of those water-soluble tracers by deep convection. But this effect will be

161 involved in the next version of BCC model.

162   The BCC-AVIM2.0 is the land model with terrestrial carbon cycle. It is described in

163 details in Li et al. (2019) and includes biophysical, physiological, and soil carbon-nitrogen

164 dynamical processes. The terrestrial carbon cycle operates through a series of biochemical

165 and physiological processes on photosynthesis and respiration of vegetation. Biogenic

166 emissions from vegetation are computed online in BCC-AVIM2.0 following the algorithm of

167 the Model of Emissions of Gases and Aerosols from Nature version 2.1 (MEGAN2.1,

168 Guenther et al., 2012).

169   The oceanic component of BCC-ESM1 is the Modular Ocean Model version 4 with 40

170 levels (hereafter MOM4-L40), and the sea ice component Sea Ice Simulator (SIS).

171 MOM4-L40 uses a tripolar grid of horizontal resolution with 1° longitude by 1/3° latitude

172 between 30°S and 30°N ranged to 1° longitude by 1° latitude from 60°S and 60°N poleward

173 and 40 z-levels in the vertical. Carbon exchange between the atmosphere and the ocean are

174 calculated online in MOM4-L40 using a biogeochemistry module that is based on the

175 protocols from the Ocean Carbon Cycle Model Intercomparison Project–Phase 2 (OCMIP2,

176 http://www.ipsl.jussieu.fr/OCMIP/phase2/). SIS has the same horizontal resolution as

177 MOM4-L40 and three layers in the vertical, including one layer of snow cover and two layers

178 of equally sized sea ice. Details of oceanic component MOM4-L40 and sea-ice component

179 SIS that are used in BCC-ESM1 may be found in Wu et al. (2013) and Wu et al. (2019).

180 In the following sub-sections, we will describe the treatments in BCC-ESM1 for 3

181 gas-phase species of DMS, SO_2 and NH_3, 13 prognostic aerosol species including sulfate

182 (SO_4^{2-}), 2 types of organic carbon (hydrophobic OC1, hydrophilic OC2), 2 types of black

183 carbon (hydrophobic BC1, hydrophilic BC2), 4 categories of soil dust (DST01, DST02,

184 DST03, DST04), and 4 categories of sea salt (SSLT01, SSLT02, SSLT03, SSLT04).

185 Concentrations of all aerosols in BCC-ESM1 are mainly determined by advective transport,

186 emission, dry deposition, gravitational settling, and wet scavenging by clouds and

187 precipitation, except for SO_4^{2-} which gas-phase and aqueous phase conversion from SO_2 are

188 also considered. The present version of aerosol scheme belongs to a bulk aerosol model and

189 mainly refers to the scheme of CAM-Chem (Lamarque et al., 2012), but the nucleation and

190 coagulation of aerosols are still ignored.

191 **2.1 SO_2, DMS, NH_3, and Sulfate**

192 SO_2 is a main sulfuric acid precursor to form aerosol sulfate SO_4^{2-}. Conversions of SO_2

193 to SO_4^{2-} occur by gas phase reactions (Table 2) and by aqueous phase reactions in cloud

194 droplets. The dry deposition velocity of SO_2 follows the resistance-in-series approach of

195 Wesely (1989) using the formula, $W_{SO2} = 1/(r_a + r_b + r_c)$, in which r_a, r_b, and r_c are the

196 aerodynamic resistance, the quasi-laminar boundary layer resistance, and the surface

197 resistance, respectively and they are interactively computed in each model time step. The loss

198 rate of SO_2 due to wet deposition is computed following the scheme in the global Community

199 Atmosphere Model (CAM) version 4, the atmospheric component of the Community Earth

200 System Model (Lamarque et al., 2012).

201   The sources of SO_2 mainly come from fuel combustion, industrial activities, and

202   volcanoes. SO_2 can also be formed from the oxidation of DMS as listed in Table 2 in which

203   their reaction rates follow CAM-Chem (Lamarque et al. 2012). The main source of DMS is

204   from oceanic emissions via biogenic processes. It is prescribed with the climatological

205   monthly data that are extracted from MOZART2 package

206   (https://www2.acom.ucar.edu/gcm/mozart-4). SO_4^{2-} is one of the prognostic aerosols in

207   BCC-AGCM3-Chem. Its treatment follows CAM4-Chem (Lamarque et al., 2012). It is

208   produced primarily by the gas-phase oxidation of SO_2 (in Table 2) and by aqueous phase

209   oxidation of SO_2 in cloud droplets. The gas phase reactions, rate constants, and gas-aqueous

210   equilibrium constants are given by Tie et al. (2001). The heterogeneous reactions of SO_4^{2-}

211   occur on all aerosol surfaces. Their treatment follows a Bulk Aerosol Model (BAM) used in

212   CAM4 (Neale et al., 2010). The heterogeneous reactions depend strongly on pH values in

213   clouds which are calculated from the concentrations of SO_2, HNO_3, H_2O_2, NH_3, O_3, HO_2, and

214   SO_4^{2-}. NH_3 is a gas tracer apart from MOZART2 (Table 1). Its sources include aircraft and

215   surface emissions due to anthropogenic activity, biomass burning, and biogenic emissions

216   from land soil and ocean surfaces (Table 4). SO_4^{2-} is assumed to be all in aqueous phase due

217   to water uptake, although Wang et al. (2008a) showed that ~34% of sulfate particles are in

218   solid phase globally due to the hysteresis effect of ammonium sulfate phase transition.

219   However, in terms of radiative forcing, consideration of solid sulfate formation process

220   lowers the sulfate forcing by ~8% as compared to consideration of all sulfate particles in

221   aqueous phase (Wang et al., 2008b). Future model development may consider the life cycle of

222   NH_3. The sulfate in- and below-cloud scavenging follows Neu and Prather (2011). Washout

223   of SO_4^{2-} is set to 20% of the washout rate of HNO_3 following Tie et al. (2005) and Horowitz

224   (2006). Dry deposition velocity of SO_4^{2-} is also calculated by the resistance-in-series

225   approach.

226   **2.2 Aerosols of organic carbon and black carbon**

227   BCC-AGCM3-Chem treats two types of organic carbon (OC), i.e. water-insoluble tracer

228   OC1 and water-soluble tracer OC2, and two types of black carbon (BC), i.e. water-insoluble

229   tracer BC1 and water-soluble tracer BC2. As shown in Table 2, hydrophobic BC1 and OC1

230   can be converted to hydrophilic BC2 and OC2 with a constant rate of 7.1×10^{-6} s^{-1} (Cooke and

231 Wilson, 1996). The 4 tracers of organic carbon and black carbon are mainly from emissions

232 including both fossil fuel and biomass burning, and are from the CMIP6 data package

233 (https://esgf-node.llnl.gov/search/input4mips/, Hoesly et al., 2018). Beside anthropogenic and

234 biomass burning emissions, hydrophilic organic carbon OC2 can also come from natural

235 biogenic volatile organic compound (VOC) emissions. Dry deposition velocities for all the 4

236 OC and BC tracers are set to 0.001m.s^{-1}. OC2 and BC2 are soluble aerosols, and their sinks

237 are primarily governed by wet deposition. Their in- and below-cloud scavenging follows the

238 scheme of Neu and Prather (2011).

239 **2.3 Sea salt aerosols**

240   As shown in Table 3, sea salt aerosols in the model are classified into four size bins (0.2–

241 1.0, 1.0–3.0, 3.0–10, and 10–20 μm) in diameter. They originate from oceans and are

242 calculated online by BCC-ESM1. The upward flux $F_{sea-salt}$ of sea salt productions for four

243 bins is proportional to the 3.41 power of the wind speed u_{10m} at 10 m height near the sea

244 surface (Mahowald et al., 2006) and is expressed as

245
$$F_{sea-salt} = S \cdot (u_{10m})^{3.41}, \tag{1}$$

246 where S is a scaling factor and set to 4.05×10^{-15}, 4.52×10^{-14}, 1.15×10^{-13}, 1.20×10^{-13} for four

247 size bins of sea salt aerosols in BCC-ESM1, respectively.

248   Dry deposition of sea salts depends on the turbulent deposition velocity in the lowest

249 atmospheric layer using aerodynamic resistance and the friction velocity, and the settling

250 velocity through the whole atmospheric column for each bin of sea salts. The turbulent

251 deposition velocity and settling velocity depend on particle diameter and density (listed in

252 Table 3). In addition, the fact that the size of sea salts changes with humidity is also

253 considered. The wet deposition of sea salts follows the scheme for soluble aerosols used in

254 CAM4, and depends on prescribed solubility and size-independent scavenging coefficients.

255 **2.4 Dust aerosols**

256   Dust aerosols behave in a similar way as sea salts. Their variations involve three major

257 processes: emission, advective transport, and wet/dry depositions. The dust emission is based

258 on a saltation-sandblasting process, and depends on wind friction velocity, soil moisture, and

259 vegetation/snow cover (Zender et al., 2003). The vertical flux of dust emission is corrected by

260 a surface erodible factor at each model grid cell which has been downloaded from NCAR

261 website (https://svn-ccsm-inputdata.cgd.ucar.edu/trunk/inputdata/atm/cam/dst/). Soil

262 erodibility is prescribed by a physically-based geomorphic index that is proportional to the

263 runoff area upstream of each source region (Albani et al., 2014). Like sea salts, dry deposition

264 of dust aerosols includes gravitational and turbulent deposition processes, while wet

265 deposition results from both convective and large scale precipitation and is dependent on

266 prescribed size-independent scavenging coefficients.

267 **2.5 Effects of aerosols on radiation, clouds, and precipitation**

268 The mass mixing ratios of bulk aerosols are prognostic variables in BCC-ESM1 and

269 directly affect the radiative transfer in the atmosphere with their treatments following the

270 NCAR Community Atmosphere Model (CAM3, Collins et al., 2004). Indirect effects of

271 aerosols are taken into account in the present version of BCC-AGCM3-Chem (Wu et al.,

272 2019). Aerosol particles act as cloud condensation nuclei and exert influence on cloud

273 properties and precipitation, and ultimately impact the hydrological cycle. Prognostic aerosol

274 masses are used to estimate the liquid cloud droplet number concentration N_{cdnc} (cm^{-3}) in

275 BCC-AGCM3-Chem. N_{cdnc} is explicitly calculated using the empirical function suggested

276 by Boucher and Lohmann (1995) and Quaas et al. (2006):

$$N_{cdnc} = \exp\left[5.1 + 0.41\ln\left(m_{aero}\right)\right] \qquad (2)$$

278 where m_{aero} ($\mu g.m^{-3}$) is the total mass of all hydrophilic aerosols,

$$m_{aero} = m_{SS} + m_{OC} + m_{SO_4} + m_{NH_4NO_2} , \qquad (3)$$

280 i.e. the first bin of sea salt (m_{SS}), hydrophilic organic carbon (m_{OC}), sulphate (m_{SO_4}), and

281 Ammonium nitrite (NH$_4$NO$_2$). A dataset of NH$_4$NO$_2$ from NCAR CAM-Chem (Lamarque et

282 al., 2012) is used in our model.

283 N_{cdnc} is an important factor in determining the effective radius of cloud droplets for

284 radiative calculation. The effective radius of cloud droplets r_{el} is estimated as

$$r_{el} = \beta \cdot r_{l,vol} , \qquad (4)$$

286 where β is a parameter dependent on the droplets spectral shape and follows the calculation

287 proposed by Peng and Lohmann (2003),

$$\beta = 0.00084 N_{cdnc} + 1.22 . \qquad (5)$$

289 $r_{l,vol}$ is the volume-weighted mean cloud droplet radius,

$$r_{l,vol} = \left[(3LWC) / (4\pi\rho_w N_{cdnc}) \right]^{1/3}, \qquad (6)$$

291 where ρ_w is the liquid water density and LWC the cloud liquid water content (g cm^{-3}).

292   Aerosols also exert impacts on precipitation efficiency (Albrecht, 1989), which is taken

293 into account in the parameterization of non-convective cloud processes. There are five

294 processes that convert condensate to precipitate: auto-conversion of liquid water to rain,

295 collection of cloud water by rain, auto-conversion of ice to snow, collection of ice by snow,

296 and collection of liquid by snow. The auto-conversion of cloud liquid water to rain (*PWAUT*)

297 is dependent on the cloud droplet number concentration and follows a formula that was

298 originally suggested by Chen and Cotton (1987),

$$PWAUT = C_{l,aut} \hat{q}_l^2 \rho_a / \rho_w \left(\frac{q_l \rho_a}{\rho_w N_{ncdc}} \right)^{1/3} H\left(r_{l,vol} - r_{lc,vol} \right) \qquad (7)$$

300 Where $\hat{q}_l$ is in-cloud liquid water mixing ratio, ρ_a and ρ_w are the local densities of air and

301 water respectively, and $C_{l,aut}$ is a constant. $H(x)$ is the Heaviside step function with the

302 definition,

$$H(x) = \begin{cases} 0, & x < 0 \\ 1, & x \geq 0 \end{cases} . \qquad (8)$$

304 $r_{lc,vol}$ is the critical value of mean volume radius of liquid cloud droplets $r_{l,vol}$, and set to 15

305 μ m.

306   The treatment of aerosol single scattering (optical) properties (such as mass extinction

307 efficiency, single scattering albedo, and asymmetric factor) follows the look-up table

308 approach in CAM (Collins et al., 2004). The optics for black, organic carbon, sea salt, and sea

309 salt particles is assumed to be same as the optics for soot and water-soluble aerosols in the

310 Optical Properties of Aerosols and Clouds (OPAC) data set (Hess et al., 1998). The optics for

311 dust is derived by Mie calculations for the size distribution represented by each size bin

312 (Zender et al., 2003). Similarly, for sulfate and nitrate particles, same set of aerosol optical

313 properties for ammonium sulfate are used and are taken from Wang et al. (2008b) with

314 treatment of aerosol hygroscopicity. The volcanic stratospheric aerosols are assumed to be

315 comprised of 75% sulfuric acid and 25% water, as in Hess et al. (1998). For each model year,

different aerosol types are assumed to be externally mixed in the calculation of bulk aerosol single scattering properties that are in turn used in the radiative transfer calculations.

3. Experiment design for the 20th century climate simulation

There is an Aerosol Chemistry Model Intercomparison Project (AerChemMIP, Collins et al., 2017) endorsed by the Coupled-Model Intercomparison Project 6 (CMIP6) for documenting and understanding past and future changes in the chemical composition of the atmosphere, and estimating the global-to-regional climate response from these changes. Modelling groups with full chemistry and aerosol models are encouraged to perform all AerChemMIP simulations (Collins et al., 2017). To assess the ability of our model to simulate aerosols (mean and variability), we have followed the historical simulation designed by CMIP6 (Eyring et al., 2016) which is named as "historical" experiment in the Earth System Grid Federation (ESGF). The historical experiment is forced with emissions evolving from 1850 to 2014 that include biomass burning emissions (Van Marle et al. 2017), anthropogenic and open burning emissions (Hoesly et al., 2018; Feng et al., 2019). O_3 in the historical simulation is an interactive prognostic variable and feedbacks on radiation, and the concentrations of other WMGHG, e.g. CH_4, N_2O, CO_2, CFC11, and CFC12 are prescribed using CMIP6 historical forcing data (Meinshausen et al., 2017). Although CH_4 and N_2O are prognostic variables in the chemistry scheme (Table 1), their prognostic values at each model step in the historical experiment are replaced by CMIP6 data (Meinshausen et al., 2017) throughout the model domain. The rest of historical forcing data include: (1) yearly global gridded land-use forcing data sets (Hurtt et al., 2011; Hurtt et al., 2017), and (2) solar forcing (Matthes et al., 2017). All these datasets were downloaded from https://esgf-node.llnl.gov/search/input4mips/. Climate feedback processes that involve changes to the atmospheric composition of reactive gases and aerosols may affect the temperature response to a given WMGHG concentration level.

3.1 Surface emissions

Surface emissions of chemical species from different sources are summarized in Table 4. They include anthropogenic emissions from fossil fuel burning and other industrial activities, biomass burning (including vegetation fires, fuel wood and agricultural burning), biogenic emissions from vegetation and soils, and oceanic emissions. Most historical

346 emissions from anthropogenic source (surface, aircraft plus ship) and biomass burning from

347 1850 to 2014 are CMIP6-recommended data (available at

348 https://esgf-node.llnl.gov/search/input4mips). Anthropogenic or biomass burning sources of

349 some tracers which are not included in the CMIP6 dataset (see Table 4), anthropogenic

350 emission of H_2 and N_2O are from monthly climatological dataset provided by the MOZART-2

351 standard package. N_2O is a prognostic variable in BCC-ESM1 but it is replaced by CMIP6

352 prescribed concentration in the historical run. Other emissions including biomass burning

353 (CH_3COCH_3) and anthropogenic emission (CH_3CHO, CH_3OH, and CH_3COCH_3) are from the

354 Atmospheric Chemistry and Climate Model Intercomparison Project (ACCMIP) emission

355 inventory (http://accent.aero.jussieu.fr/ACCMIP.php) covering the period from 1850 to 2010

356 with 10-year intervals (see Table 4). Monthly lumped emissions of black carbon and organic

357 carbon aerosols from 1850 to 2014 are downloaded from CMIP6-recommended data, but we

358 used 80% (for BC) and 50% (for OC) of them in their hydrophobic forms (BC1 and OC1) and

359 the rest in their hydrophilic forms (BC2 and OC2), following the work of Chin et al. (2002).

360 Five tracers of ISOP, ACET (CH_3COCH_3), C_2H_4, C_3H_8, and Monoterpenes ($C_{10}H_{16}$) in

361 Table 1 belong to biogenic volatile organic carbons (VOCs). As shown in Table 4, those

362 VOCs emissions are online calculated in BCC-ESM1 following the modeling framework of

363 the Model of Emissions of Gases and Aerosols from Nature version 2.1 (MEGAN2.1,

364 Guenther et al., 2012) using simple mechanistic algorithms to account for major known

365 processes controlling biogenic emissions. The MEGAN2.1 can provide a flexible scheme for

366 estimating 16 tracers of biogenic emissions from terrestrial ecosystems including five VOCs

367 emissions used in BCC-ESM1 (Table 4). All the VOCs emissions depend on current and past

368 surface air temperature, solar flux, and the landscape types. Their calculation requires global

369 maps of plant functional type (PFT) and leaf area index (LAI) which is a prognostic variable

370 from the land model BCC-AVIM2. The effect of atmospheric CO_2 concentration on isoprene

371 emissions is included. 10% of the biogenic monoterpenes emissions as calculated online with

372 the MEGAN2.1 algorithm in BCC-AVIM2 are converted to hydrophilic organic carbon (OC2)

373 to account for formation of secondary organic aerosols following Chin et al. (2002) in this

374 version of BCC-ESM1.

375 **3.2 Volcanic eruptions, lightning and aircraft emissions**

376   As there is no stratospheric aerosol scheme in BCC-ESM1, concentrations of sulfate

377   aerosol at heights from 5 to 39.5 km, which volcanic origin, are directly prescribed using the

378   CMIP6-recommended data (Thomasson et al., 2018) from 1850 to 2014. The effects of

379   surface SO_2 emissions from volcanic eruption on the variation of SO2 in the atmosphere and

380   then on the variation of tropospheric SO_4^{2-} concentration are considered, and the SO_2

381   emissions from 1850 to 2014 are downloaded from the IPCC ACCMIP emission inventory

382   (http://accent.aero.jussieu.fr/ACCMIP.php). Aircraft emissions are provided for NO_2, CO,

383   CH_4, NH_3, NO, SO_2, and aerosols of OC and BC (Table 1). The emissions of NO from

384   lightning are online calculated in BCC-AGCM3-Chem following the parameterization in

385   MOZART2, and the globally-averaged mean during the period of 1850 to 2014 is 5.19

386    $Tg(N) yr^{-1}$, which is in agreement with observations within the range of 3 to 6 $Tg(N) yr^{-1}$

387   (Martin et al., 2002). The lightning frequency depends strongly on the convective cloud top

388   height, and the ratio of cloud-to-cloud versus cloud-to-ground lightning depends on the cold

389   cloud thickness from the level of 0℃ to the cloud top (Price and Rind, 1992).

390   **3.3 Upper boundary of the atmosphere**

391   As no stratospheric chemistry is included in the present version of BCC-AGCM3-Chem,

392   it is necessary to ensure a proper distribution of chemically-active stratospheric species.

393   Concentrations of different tracers (O_3, CH_4, N_2O, NO, NO_2, HNO_3, CO, and N_2O_5) at the top

394   two layers of the model are set to prescribed monthly climatological values, and

395   concentrations from below the top two layers to the tropopause are relaxed at a relaxation

396   time of 10-days towards the climatology. Climatological values of NO, NO_2, HNO_3, CO and

397   N_2O_5 at the top two layers are extracted from MOZART2 data package available at the

398   Website (https://www2.acom.ucar.edu/gcm/mozart-4), originated from the Study of Transport

399   and Chemical Reactions in the Stratosphere (STARS, Brasseur et al., 1997). Concentrations

400   for the other tracers (O_3, CH_4, and N_2O) at the top two model layers are the zonally-averaged

401   and monthly values from 1850 to 2014 derived from the CMIP6 data package.

402   **3.4 The preindustrial model states**

403   The preindustrial state of BCC-ESM1 is obtained from a piControl simulation of over 600

404   years in which all forcings including emissions data are fixed at 1850 conditions. The initial

405   state of the piControl simulation itself is obtained through individual spin-up runs of each

406 component of BCC-ESM1 in order for the piControl simulation to run stably and fast to reach

407 its equilibrium. Figures 1(a-c) show the time series of global yearly means of the net energy

408 budget at top of the atmosphere (TOA), near-surface air temperature (TAS), and sea surface

409 temperature (SST) from the piControl simulation for the last 450 years. It shows that the

410 surface climate in BCC-ESM1 nearly reaches its equilibrium after 600 years piControl

411 simulation. The whole system in BCC-ESM1 fluctuates around +0.7 Wm^{-2} net energy flux at

412 TOA without obvious trend in 450 years (Fig. 1a). This level of TOA energy imbalance is

413 close to the average imbalance (1.0 Wm^{-2}) among CMIP5 models (Wild et al., 2013). It means

414 that there exists surplus energy of +0.7 Wm^{-2} obtained by the whole system in BCC-ESM1,

415 but do not cause remarkable climate drift. The global mean TAS and SST keep around 288.1

416 K (Fig. 1b) and 295.05 K (Fig. 1c), respectively. During the last 450 years, there are (±0.2 K

417 amplitude of TAS and SST) oscillations of centennial scale for the whole globe (Figs. 1b and

418 1c), which are certainly caused by internal variation of the system.

419   Figures 2a-2c show the time series of global annual total burdens of SO_2, DMS, and OH

420 in the troposphere (integrated from the surface to 100 hPa) in the last 450 years of the

421 piControl simulation. Without any anthropogenic source, the SO_2 amount in the troposphere

422 nearly keeps the level of 0.0868 Tg in the 450 years of the piControl simulation. Tropospheric

423 DMS varies around the value of 0.116 Tg. Tropospheric OH, as an important gas species

424 oxidizing SO_2 to form SO_4^{2-} (Table 2), keeps at a stable level in the atmosphere. SO_4^{2-} also

425 remains at a stable level of 0.556 Tg in the atmosphere in the whole period of the piControl

426 simulation (Figure 2d). The amounts of BC and OC in the troposphere vary around 0.0395 Tg

427 and 0.275 Tg (Figures 2e-2f), respectively. Dust and sea salt aerosols are at the level of 22 Tg

428 and 11.7 Tg (Figures 2g-2h), respectively. All those data are close to the global mean

429 concentrations of 0.604 Tg SO_4^{2-}, 0.046 Tg BC, 0.30 Tg OC, 22.18 Tg dust, and 11.73 Tg sea

430 salts in 1850 which are estimated based on the CMIP5 prescribed data in 1850 (Lamarque et

431 al., 2010).

432   Figure 3 shows the global spatial distributions of annual mean sulfate, organic carbon,

433 black carbon, dust, and sea salt aerosols in the whole atmospheric column averaged for the

434 last 100 years of the piControl simulation of BCC-ESM. We can compare them with CMIP5

435 recommended concentrations in year 1850, considered as the reference state in the

436   pre-industrial stage. At that time, there are fewer anthropogenic/biomass SO_2 emissions, the

437   SO_4^{2-} over land are evidently smaller than those over oceans especially over the tropical

438   Pacific and Atlantic Oceans, where DMS can be oxidized to SO_2 and then form SO_4^{2-}. There

439   are several centers of high values of black carbon and organic carbon in East and South Asia,

440   Europe, Southeast America, and in the tropical rain forests in Africa and South America.

441   They mainly result from biomass burning including vegetation fires, fuel wood and

442   agricultural burning. Dust aerosols are mainly distributed in North Africa, Central Asia, North

443   China, and Australia, where arid and semi-arid areas locate. Dust emitted from Sahara Desert

444   can be transported to the tropical Atlantic by easterly wind. The sea salt aerosols are mainly

445   distributed over the mid-latitude Southern Oceans, the tropical southern Indian Ocean, and the

446   tropical northern Pacific Ocean, where wind speeds near the sea surface are strong. As shown

447   in Fig. 3, all the spatial distribution patterns of CMIP5-derived sulfate, black carbon, organic

448   carbon, dust, and sea salt aerosols (Lamarque et al., 2010) are well simulated in BCC-ESM1.

449   There are high spatial correlation coefficients, 0.76 for sulfate, 0.77 for black carbon, 0.77 for

450   organic carbon, 0.94 for dust, and 0.94 for sea salts, between CMIP5 data and BCC-ESM1

451   simulations. Relative lower relations for sulfate, black carbon and organic carbon are possibly

452   caused as different anthropogenic emission sources are used in BCC-ESM1 and to create

453   CMIP5 data. Dust and sea salts belong to natural aerosols and depend on the land and sea

454   surface conditions, so their spatial distributions are easy to be captured and have relatively

455   higher correlations between CMIP5 data and BCC-ESM1 simulations.

456

457   **4. Evaluation of O_3 and aerosol simulations in the 20th century**

458   The rate of sulfate formation is dependent on the levels of oxidants in the troposphere.

459   O_3 is an important oxidant. So, the evaluation of simulated tropospheric O_3 is helpful to

460   understand   the   aerosols   simulations.   BCC-ESM1   is   driven   by   most   of   the

461   CMIP6-recommended emission data. As shown in Figure 4, the zonal distributions of the total

462   amounts of tropospheric O_3 below 300 hPa to the ground and their changes with time from

463   1850 to 2014 from the CMIP6-recommend dataset (Table 4) are well simulated by

464   BCC-ESM1. Evident increasing trends since 1850 almost exist in every latitudes, especially

465   in the Northern Hemisphere where the contents of tropospheric O_3 are higher than those in the

466   Southern Hemisphere.

467   Figure 5 shows the vertical profiles of O_3 simulations with comparison to global

468   ozonesonde observations averaged for the monthly data over 2010-2014 from the World

469   Ozone and Ultraviolet Radiation Data Centre (WOUDC; http://woudc.org/data.php, last

470   access: 24 September 2019) in nine regions which are averaged from 41 global WOUDC sites.

471   The details of WOUDC data may refer to Lu et al. (2019). As shown in Figure 5, BCC-ESM1

472   well captures the observed ozone vertical structure at all regions. At the lower and middle

473   troposphere (i.e. below 6 km), the model typically shows positive bias within 5 ppbv for the

474   Southern Hemisphere and 10 ppbv for the Northern mid-latitudes, similar to those simulated

475   from many other global atmospheric chemical models (Young et al., 2013, 2018). The model

476   has larger ozone overestimation in the upper troposphere and stratosphere at most regions, at

477   least partly due to the use of prescribed stratospheric ozone as upper boundary conditions

478   and/or errors in modeling ozone exchange between the stratosphere and the troposphere.

479   Global tropospheric ozone burden derived from our simulation is 335 Tg averaged over

480   2010-2014, in consistent with recent assessment from multi chemistry models (Young et al.,

481   2018).

482   **4.1 Global aerosols trends**

483   Figure 6(a)-(c) show the time series of global total emissions of SO_2, OC, and BC to the

484   atmosphere from natural and anthropogenic sources. Emissions of SO_2 are largely due to

485   industrial production. From 1850 to 1915, SO_2 emissions increased year by year as the

486   Industrial Revolution intensified and expanded. But from 1915 to 1945, the increase trend of

487   SO_2 emissions became slower as broke out the First and the Second World Wars. After that

488   period, with growing industrial productions, SO_2 emissions increased again and reached a

489   maximum around the end of 1970s. During the 1980s and 2000s, with a substantial decrease

490   of SO_2 emissions in Europe and the United States, the global SO_2 emissions has been

491   decreasing since the 1980s despite the rapid increase of SO_2 emissions in South and East Asia

492   as well as in developing countries in the Southern Hemisphere in recent years (Liu et al.,

493   2009). The OC and BC emissions substantially increased since 1950s just after the Second

494   World War. The global total OC emission in 2010 was nearly twice as much as that in

495   pre-industrial (year 1850) and increased by 18 Tg $\cdot$ yr^{-1}. Anthropogenic black carbon

496   emissions increased from 1 Tg yr^{-1} in 1850 to nearly 8 Tg yr^{-1} in 2010.

497   Anthropogenic SO_2, OC and BC emissions strongly affect the variations of atmospheric

498   concentrations of sulfate, OC, and BC. The global 0.5^ox0.5^o gridded data of

499   CMIP5-recommended aerosols masses with 10-years interval from 1850 to 2000 (Lamarque

500   et al., 2010) provides an important reference to evaluate the aerosol simulations in

501   BCC-ESM1. As shown in Figure 7b-7f, the annual total aerosol burdens of SO_4^{2-}, OC, and BC

502   in the whole atmosphere column as simulated by the BCC-ESM1 20th century historical

503   simulation are generally consistent with the values derived from CMIP5-recommended

504   aerosols concentrations. Due to increasing SO_2 emissions from 1850 to present day (Fig. 6),

505   the global SO_2 burden in the atmosphere increased from 100 Tg in 1850s to 200 Tg in 1980s

506   (Fig. 7a), and has a high correlation coefficient of 0.996 with the anthropogenic emissions

507   (Fig. 6a), as the lifetime of SO_2 is short. The burden directly followed the emission. DMS in

508   the atmosphere is oxidized by OH and NO_3 to form SO_2 (Table 2). Its natural emissions from

509   oceans from 1850 to 2010 in the model are the climatological monthly means (Dentener et al.,

510   2006) from MOZART2 data package. As shown in Fig 7a, the global amount of DMS in the

511   whole atmosphere was about 0.12 Tg during 1850-1900 and decreased to 0.055 Tg in 2010.

512   This decrease trend maybe partly results from the speeded rate of DMS oxidation with global

513   warming, and the loss of DMS gradually exceeds the source of ocean DMS emission to cause

514   a net loss of DMS in the atmosphere since 1910s. Largely driven by SO_2 anthropogenic

515   emissions, the sulfate burden shows three different stages from 1850 to present. In the first

516   period from 1850s to 1900s, the sulfate burden had a weak linear increase. It increased

517   significantly in the second stage from 1910's to 1940's, and then exploded since 1950's, until

518   the middle 1970s and early 1980s. The sulfate burden then remained nearly stable and even

519   showed slightly decreases as seen from the CMIP5 data. As for global BC and OC burdens,

520   BCC-ESM1 results show continuous increases since 1850s, especially from 1950 to present.

521   From 1910's to 1940's, the CMIP5 data show a slight decrease of BC and OC burdens in the

522   atmosphere.

523   The dust and sea salt aerosols in the atmosphere are largely determined by the

524   atmospheric circulations and states of the land and ocean surface. We can see that the global

525   dust burden in the atmosphere showed evident increase from 1980 to 2000, which could be

526 partly caused by evident global warming since 1980 and increasing soil dryness resulting in

527 more surface dust to be released in the atmosphere. Their details will be explored in the other

528 paper.

529 **4.2 Global aerosols budgets**

530   We further evaluate global aerosols budgets by comparing a 10-year average of

531 BCC-ESM results from 1990 to 2000 with various studies for sulfate, BC, OC, sea salt, and

532 dust. Their annual total emissions, average atmospheric mass loading, and mean lifetimes are

533 listed in Tables 5 and 6. It is worth emphasizing that the global mean total source and sink for

534 each type of aerosols in BCC-ESM1 are almost balanced.

535   The global DMS emission from the ocean is 27.4 $Tg(S)\ yr^{-1}$ in BCC-ESM. This

536 emission in BCC-ESM is nearly balanced by the gas-phase oxidation of DMS to form SO_2.

537 The DMS burden is 0.12 Tg with a lifetime of 0.78 days, which is within the range of other

538 models reported in the literature. As shown in Table 5, the total SO_2 production averaged for

539 the period of 1991 to 2000 is 76.93 $Tg(S)\ yr^{-1}$. A rate of 13.2 $Tg(S)\ yr^{-1}$ (about 17%) SO_2 is

540 produced from the DMS oxidation, only 0.1 $Tg(S)\ yr^{-1}$ SO_2 from airplane emissions to the

541 atmosphere, and the rest (63.63 $Tg(S)\ yr^{-1}$, near 82.7%) from anthropogenic activities and

542 volcanic eruption at surface. The amount of SO_2 produced from the DMS oxidation is in the

543 range of other works (10.0 to 24.7 $Tg(S)\ yr^{-1}$) reported in Liu et al (2005). All the SO_2

544 production is balanced by SO_2 losses by dry and wet deposition, and by gas- and

545 aqueous-phase oxidation. Half of its loss (38.74 $Tg(S)\ yr^{-1}$) occurs via its aqueous-phase

546 oxidation to form sulfate. Other losses through dry and wet depositions and gas-phase

547 oxidation to form SO_4^{2-} are also important (Table 2). All the sinks are in the range from the

548 literature (Liu et al., 2005). The global burden of SO_2 in the atmosphere is 0.48 Tg with a

549 lifetime of 1.12 days, consistent with values in literature (Liu et al., 2005).

550   Sulfate aerosol is mainly produced from aqueous-phase SO_2 oxidation (38.73 $Tg(S)\ yr^{-1}$)

551 and partly from gaseous phase oxidation of SO_2 (10.32 $Tg(S)\ yr^{-1}$), and is largely lost by wet

552 scavenging (49.06 $Tg(S)\ y^{r-1}$). The total SO_4^{2-} production in BCC-ESM is at the lower range

553 of values in other models reported in Textor et al. (2006). Its global burden is 1.89 Tg and the

554 lifetime is 4.69 days, which are within the range of 1.71 to 2.43 Tg and 3.3 to 5.4 days in the

555 literatures (Textor et al., 2006; Liu et al., 2012; Liu et al., 2016; Matsui and Mahowald, 2017;

556   Tegen et al., 2019; the value derived from CMIP5 data).

557   Sources of BC and OC are mainly from anthropogenic emissions. Based on the CMIP6

558   data, there are, on average, 7.22 Tg yr^{-1} BC and 13.91 Tg yr^{-1} OC from fossil and bio-fuel

559   emissions and 18.38 Tg yr^{-1} OC from natural emission during the period of 1991 to 2000.

560   Most of them are scavenged through convective and large-scale rainfall processes. The rest

561   returns to the surface by dry deposition. The simulated global BC and OC burdens are 0.13

562   and 0.62 Tg, respectively (Table 6), all close to values of 0.114 Tg BC and 0.69 Tg OC

563   derived from the CMIP5 data, and within the range of 0.11-0.26 Tg BC (Textor et al., 2006;

564   Matsui and Mahowald, 2017; Tegen et al., 2019) and less than the values of 1.25-2.2 Tg OC

565   in other literatures (Textor et al., 2006; Tegen et al., 2019). The simulated BC and OC

566   lifetimes are 6.6 and 5.0 days respectively, and are close to the recent values of 5.0-7.5 days

567   BC and 5.4-6.6 days OC in literatures (Matsui and Mahowald, 2017; Tegen et al., 2019).

568   The emissions of dust and sea salt are mainly determined by winds near the surface. The

569   annual total dust emission in BCC-ESM1 is 2592 Tg yr^{-1}, higher than AeroCom multi-model

570   mean (1840 Tg yr^{-1}, Textor et al., 2006), but comparable to other studies (Chin et al., 2002;

571   Liu et al., 2012; Matsui and Mahowald, 2017). The average dust loading is 22.93 Tg, lower

572   than the value of 35.9 Tg in Ginoux et al. (2001) but slightly higher than the value of 20.41

573   Tg derived from CMIP5 data. The average lifetime for dust particles is 3.23 days that is

574   shorter than the AeroCom mean (4.14 days) and the value of 3.9 days in recent study (Matsui

575   and Mahowald, 2017). The simulated sea salt emission is 4667.2 Tg yr^{-1}, slightly lower than

576   the simulated value in Liu et al. (2012), and substantially lower than the AeroCom mean

577   (16600 Tg yr^{-1}, Textor et al., 2006). The simulated sea salt burdens are 11.89 Tg and close to

578   the CMIP5 data. Their averaged lifetimes are 0.93 days and close to the value in the recent of

579   Matsui and Mahowald (2017) but longer than the AeroCom mean (0.41days, Textor et al.,

580   2006).

581   **4.3 Global aerosol distributions at present day**

582   Figures 8-12 show December-January-February (DJF) and June-July-August (JJA) mean

583   column mass concentrations of sulfate (SO_4^{2-}), OC, BC, Dust, and Sea Salt aerosols averaged

584   for the period of 1991-2000, respectively. Here, BCC-ESM1 simulated results are compared

585   with the CMIP5-recommended data for the same period. Unlike the pre-industrial level of

586   sulfate shown in Fig. 2, sulfate concentrations at present day (Fig. 8) are strongly influenced

587   by anthropogenic emissions, and have maximum concentrations in the industrial regions (e.g.,

588   East Asia, Europe, and North America). Their seasonal variations are distinct and are

589   characterized by high concentrations in boreal summer and low concentrations in boreal

590   winter. These spatial distributions simulated by BCC-ESM1 are well consistent with the

591   CMIP5 data, with spatial correlation coefficients in DJF and JJA reaching 0.92 and 0.83

592   (Figure 13), respectively. The deviation of the spatial pattern in BCC-ESM1 is less from the

593   CMIP5 data in DJF but larger in JJA (Figure 13).

594   Unlike sulfate whose maximum concentrations are mainly distributed between 60 ˚N

595   and the equator, peaking concentrations of BC and OC as shown in Figs. 9 and 10 are located

596   near the tropics in the biomass burning regions (e.g., the maritime continent, Central Africa,

597   South America), and their seasonal variations from DJF to JJA are evidently weaker than

598   those of sulfate except in South America. In boreal summer, there are centers of high values

599   in the industrial regions in the Northern Hemisphere mid-latitudes (i.e., East Asia, South Asia,

600   Europe, and North America). These main features of spatial and seasonal variations in CMIP5

601   data are well captured by BCC-ESM1, and the BCC-ESM1 vs. CMIP5 spatial correlation

602   coefficients (Figure 13) are 0.90 (OC in DJF), 0.91 (BC in DJF), 0.91 (OC in JJA) and 0.92

603   (BC in JJA). There are less deviations of spatial pattern for OC in DJF and JJA, but larger

604   deviation for BC from CMIP5 data (Figure 13).

605   As show in Figure 11, dust concentrations in the atmosphere show largest values over

606   strong source regions such as Northern Africa, Southwest and Central Asia, and Australia,

607   and over their outflow regions such as the Atlantic and the western Pacific. In DJF, the

608   CMIP5 data shows centers of high concentrations over East Asia and Central North America,

609   but both centers are missing in BCC-ESM1. However, these two high-value centers in the

610   CMIP5 data may not be true, since frozen soils in these areas in winter lead to unfavorable

611   conditions for soil erosion by winds. The spatial correlation coefficients between CMIP5 and

612   BCC-ESM1 remain high: 0.95 in JJA and 0.88 in DJF (Figure 13). Small deviations of spatial

613   pattern for dust simulations in BCC-ESM1 show less magnitude of dust maximums against

614   with CMIP5 data (Figure 13).

615   As shown in Figure 12, high sea salt concentrations are generally over the storm track

616   regions over the oceans, e.g., mid-latitudes in the Northern Oceans in DJF and the Southern

617   Ocean in JJA where wind speeds and thus sea salt emissions are higher. In addition, there is a

618   belt of high sea salt concentrations in the subtropics of both hemispheres where precipitation

619   scavenging is weak. Their spatial distributions in BCC-ESM1 are consistent with the CMIP5

620   data with correlation coefficients of 0.92 in JJA and 0.90 in DJF (Figure 13). The spatial

621   deviations of sea salt are much closer to CMIP5 data than those of sulfate, OC, BC, and dust

622   distributions (Figure 13).

623   Figure 14 shows vertical distributions of zonally-averaged annual mean concentrations

624   of sulfate, organic carbon, black carbon, dust, and sea salt aerosols in the period of 1991-2000.

625   Both BCC-ESM1 and CMIP5 results show that strong sulfur, OC, and BC emissions in the

626   industrial regions of the Northern Hemisphere mid-latitudes can rise upward and be

627   transported towards the North Pole in the mid- to upper troposphere. Most of OC, BC, and

628   dust aerosols are confined below 500 hPa, while sulfate can be transported to higher altitudes.

629   Sea salt aerosols are mostly confined below 700 hPa, as the particles are large in size and

630   favorable for wet removal and gravitational settling towards the surface. It can be seen that

631   BCC-ESM1 tends to simulate less upward transport of aerosols than the CMIP5 data, likely

632   reflecting the omission of deep convection transport of tracers in BCC-ESM1.

633   The CMIP5 data used here are mainly from model simulations. We will further evaluate

634   the BCC-ESM1 model results with ground observations. Annual mean SO_4^{2-}, BC and OC

635   aerosol observations from the Interagency Monitoring of Protected Visual Environments

636   (IMPROVE)   sites   over   1990-2005   in   the   United   States

637   (http://vista.cira.colostate.edu/IMPROVE/) and from the European Monitoring and Evaluation

638   Programme (EMEP) (http://www.emep.int) sites over 1995-2005 are used. As shown in

639   Figure 15a and 15b, the BCC-ESM simulated sulfate concentrations are in general

640   comparable to the EMEP observations in Europe, but are systematically by about 1 μg m^{-3}

641   higher than the U.S. IMPROVE observations. As for BC, there are large model biases at both

642   European and U.S. sites (Figs. 15c and 15d), especially BCC-ESM overestimates BC

643   concentrations at the IMPROVE sites. The observed OC concentrations are slightly

644   overestimated for IMPROVE sites but systematically underestimated for EMEP sites. Some

645   statistical features for simulated concentrations versus EMEP and IMPROVE observations are

646 listed in Table 7. These comparisons are overall fairly reasonable considering the
647 uncertainties in emissions and the coarse model resolution.

648 We then evaluate the simulated BC concentrations from BCC-ESM1 with the HIAPER
649 (High-Performance Instrumented Airborne Platform for Environmental Research)
650 Pole-to-Pole Observations (HIPPO) (Wofsy et al., 2011). The HIPPO campaign provided
651 observations of black carbon concentration profiles over Pacific Ocean and North America
652 between 2009 and 2011. Following Tilmes et al. (2016), model results here are sampled along
653 the HIPPO flight tracks and then averaged to different latitude and altitude bands for
654 comparison. As shown in Figure 16, BCC-ESM1 and HIPPO aircraft observations shows
655 reasonable agreement in terms of the spatial distributions and seasonal variations of BC levels.
656 BCC-ESM1 generally reproduces the observed hemispheric gradients of BC, i.e. the larger
657 burden in the NH compared to the SH, in consistent with Figures 10 and 14. The mean value
658 of modelled results along the flight track is 11.1 ng/kg, comparable to 8.2 ng/kg of the HIPPO
659 observations. The model shows large overestimations of BC observations over the tropics,
660 which is also found in the CAM4-chem global chemical model (Tilmes et al., 2016).

661 **4.4 Aerosol Optical Properties**

662 Aerosol optical depth (AOD) is an indicator of the reduction in incoming solar
663 radiation (at a particular wavelength) due to scattering and absorption of sunlight by aerosols.
664 In this study, we calculate the AOD at 550 nm for all aerosols including sulfate, BC, organic
665 carbon, sea salt and dust as the product of aerosol dry mass concentrations, aerosol water
666 content, and their specific extinction coefficients. The total AOD is calculated by summing
667 the AOD in each model layer for each aerosol species using the assumption that they are
668 externally mixed. The AOD observations retrieved from MODIS and MISR over the period of
669 1997-2003, and from AERONET over the period of 1998–2005 (http://aeronet.gsfc.nasa.gov)
670 are used to evaluate the averaged AOD at 550 nm in BCC-ESM. Figure 17 shows averages of
671 MISR and MODIS AOD with corresponding averages from BCC-ESM. The BCC-ESM1
672 simulated AOD generally captures the spatial distribution of MISR and MODIS retrievals.
673 The model overestimates AOD over East China. It also systematically underestimates the
674 MODIS observations in the Southern Hemisphere, but is closer to MISR observations. Figure

18 shows multi-years annual means of BCC-ESM1 simulated AOD values versus observations from AERONET over the period of 1998–2005. The basic pattern of modeled global AOD is similar to that of observations and their spatial correlation reaches 0.56. Large values of AOD are mainly distributed in land continents such as North African, South Asia, East Asia, Europe, and eastern part of North America. Figures 19a-19d present scatter plots of observed versus simulated multi-year monthly mean AOD at those sites of AERONET in Europe, North America, East Asia, and South Asia over the period of 1998-2005, respectively. Model simulated monthly AOD generally agrees with observations within a factor of 2 for most sites. BCC-ESM slightly overestimates the AOD in European and North American sites. In those regions, BCC-ESM also slightly overestimates MODIS and MISR AOD observations (Fig. 17).

5. Summary and discussions

This paper presents a primary evaluation of aerosols simulated in version 1 of the Beijing Climate Center Earth System Model (BCC-ESM1) with the implementation of the interactive atmospheric chemistry and aerosol based on the newly developed BCC-CSM2. Global aerosols (including sulfate, organic carbon, black carbon, dust and sea salt) and major greenhouse gases (e.g., O_3, CH_4, N_2O) in the atmosphere can be interactively simulated when anthropogenic emissions are provided to the model. Concentrations of all aerosols in BCC-ESM1 are determined by the processes of advective transport, emission, gas-phase chemical reactions, dry deposition, gravitational settling, and wet scavenging by clouds and precipitation. The nucleation and coagulation of aerosols are ignored in the present version of BCC-ESM1. Effects of aerosols on radiation, cloud, and precipitation are fully included.

We evaluate the performance of BCC-ESM1 in simulating aerosols and their optical properties in the 20th century following CMIP6 historical simulation according to the requirement of the AerChemMIP. It is forced with anthropogenic emissions evolving from 1850 to 2014 but some WMGHGs such as CH_4, N_2O, CO_2, CFC11 and CFC12 are prescribed using CMIP6 prescribed concentrations (to replace prognostic values of CH_4 and N_2O from the chemistry scheme). Both direct and indirect effects of aerosols are considered in BCC-ESM1. Initial conditions of the CMIP6 historical simulation are obtained from a 600-year piControl simulation in the absence of anthropogenic emissions, which well captures

705   the pre-industrial concentrations of SO_4^{2-}, organic carbon (OC), black carbon (BC), dust, and

706   sea salt aerosols and are consistent with the CMIP5 recommended concentrations for the year

707   1850. With the CMIP6 anthropogenic emissions of SO_2, OC, and BC from 1850 to 2014 and

708   their natural emissions implemented in BCC-ESM1, the model simulated SO_4^{2-}, BC, and OC

709   aerosols in the atmosphere are highly correlated with the CMIP5-recommended data. The

710   long-term trends of CMIP5 aerosols from 1850 to 2000 are also well simulated by

711   BCC-ESM1. Global budgets of aerosols were evaluated through comparisons of BCC-ESM1

712   results for 1990-2000 with reports in various literatures for sulfate, BC, OC, sea salt, and dust.

713   Their annual total emissions, atmospheric mass loading, and mean lifetimes are all within the

714   range of values reported in relevant literature. Evaluations of the spatial and vertical

715   distributions of BCC-ESM1 simulated present-day SO_4^{2-}, OC, BC, Dust, and sea salt aerosol

716   concentrations against the CMIP5 datasets and in-situ measurements of surface networks

717   (IMPROVE in the U.S. and EMEP in Europe), and HIPPO aircraft observations indicate good

718   agreement among them. The BCC-ESM1 simulates weaker upward transport of aerosols from

719   the surface to the middle and upper troposphere (with reference to CMIP5-recommended

720   data), likely reflecting a lack of deep convection transport of chemical species in the present

721   version of BCC-ESM1. The AOD at 550 nm for all aerosols including sulfate, BC, OC, sea

722   salt, and dust aerosols was further compared with the satellite AOD observations retrieved

723   from MODIS and MISR and surface AOD observations from AERONET. The BCC-ESM1

724   model results are overall in good agreement with these observations within a factor of 2. All

725   these comparisons demonstrate the success of the implementation of interactive aerosol and

726   atmospheric chemistry in BCC-ESM1.

727   This work has only evaluated the ability of BCC-ESM1 to simulate aerosols. The

728   variations of aerosols especially for sulfate are related to other gaseous tracers such as OH

729   and NO_3 (Table 2), which are determined by the MOZART2 gaseous chemical scheme as

730   implemented in BCC-ESM1, and require further evaluation. As limited length of the text, the

731   other optical feature of aerosols such as extinction coefficients, single scattering albedo and

732   asymmetry parameters, and even their feedbacks on radiation and global temperature change

733   will be explored in the other paper. O_3 is evaluated in this work. Other GHGs such as CH_4 and

734   N_2O concentrations can be simulated when forced with emissions and their simulations also

735   need to be evaluated in future.

736 **6. Code and data availability**

737   The source codes of BCC-ESM1, model input files, and scripts to reproduce the

738 simulations that are presented in the article have been archived and made publicly available

739 for downloading from https://zenodo.org/record/3609337 (Wu et al., 2020). Model output of

740 BCC CMIP6 AerChemMIP simulations described in this paper refer to Zhang et al. (2019)

741 and is distributed through ESGF and freely accessible through the ESGF data portals after

742 registration. Details about ESGF are presented on the CMIP Panel website at

743 http://www.wcrp-climate.org/index.php/wgcm-cmip/about-cmip.

744

745 **Author contributions**

746   Tongwen Wu led the BCC-ESM1 development. All other co-authors have contributions

747 to it. Fang Zhang and Jie Zhang designed the experiments and carried them out. Tongwen Wu,

748 Laurent Li, Lin Zhang, Xiaohong Liu, Aixue Hu, and Jun Wang wrote the final document

749 with contributions from all other authors.

750

751 **Acknowledgements**

752 This work was supported by The National Key Research and Development Program of China

753 (2016YFA0602100). All the figures are created by the NCAR Command Language (Version

754 6.6.2) [Software].

755

756 **References**

757 Albani, S., Mahowald, N. M., Perry, A. T., Scanza, R. A., Zender, C. S., Heavens, N. G.,

758   Maggi, V., Kok, J. F., and Otto-Bliesner, B. L.: Improved dust representation in the

759   Community Atmosphere Model, J. Adv. Model. Earth Syst., 6, 541–570,

760   doi:10.1002/2013MS000279, 2014.

761 Albrecht, B.: Aerosols, cloud microphysics, and fractional cloudiness, Science, 245, 1227–

762   1230, 1989.

763   Arora, V., Boer, G., Friedlingstein, P., Eby, M., Jones, C., Christian, J., Bonan, G., Bopp, L.,

764   Brovkin, V., Cadule, P., Hajima, T., Ilyina, T., Lindsay, K., Tjiputra, J., and Wu, T.:

765   Carbon-concentration and carbon-climate feedbacks in CMIP5 Earth system models. J.

766   Climate, 26, 5289–5314, 2013.

767   Austin, J., Butchart, N., and Shine, K. P.: Possibility of an Arctic ozone hole in a

768   doubled-CO2 climate, Nature, 360, 221–225, 1992

769   Barth, M.C., Rasch, P.J., Kiehl, J.T., Benkowitz, C.M., and Schwartz, S.E.: Sulfur chemistry

770   in the National Center for Atmospheric Research Community Climate Model:

771   Description, evaluation, features, and sensitivity to aqueous chemistry. J. Geophys. Res.,

772   105, D1, 1387-1415, 2000.

773   Bey I., Jacob, D. J., Yantosca, R. M., Logan, J. A., Field, B., Fiore, A. M., Li, Q., Liu, H.,

774   Mickley, L. J., and Schultz, M.: Global modeling of tropospheric chemistry with

775   assimilated meteorology: Model description and evaluation, J. Geophys. Res., 106,

776   23,073-23,096, 2001

777   Boucher, O., Lohmann, U.: The sulphate-CCN-cloud albedo effect – a sensitivity study with

778   two general circulation models, Tellus 47B, 281–300, 1995.

779   Brasseur, G. P., Hauglustaine, D. A., Walters, S., Rasch, P. J., Mu ̈ller, J.-F., Granier, C., and

780   Tie, X. X.: MOZART, a global chemical transport model for ozone and related chemical

781   tracers: 1. Model description, J. Geophys. Res., 103, 28,265– 28,289, 1998.

782   Brasseur, G. P., Tie, X. X., Rasch, P. J., and Lef ̀evre, F.: A three‐dimensional simulation of

783   the Antarctic ozone hole: Impact of anthropogenic chlorine on the lower stratosphere and

784   upper troposphere, J. Geophys. Res., 102, 8909–8930, 1997.

785   Cariolle, D., Lasserre-Bigorry, A., and Royer, J.-F.: A general circulation model simulation of

786   the springtime Antarctic ozone decrease and its impact on midlatitudes, J. Geophys. Res.,

787   95, 1883–1898, 1990.

788   Cess, R. D.: Nuclear war: Illustrative effects of atmospheric smoke and dust upon solar

789   radiation, Clim. Change, 7, 237–251, 1985.

790   Chen, C., and Cotton, W. R.: The physics of the marine stratocumulus-capped mixed layer, J.

791   Atmos. Sci., 44 (50), 2951–2977, 1987.

792   Chin, M., Ginoux, P., Kinne, S., Torres, O., Holben, B.N., Duncan, B.N., Martin, R.V., Logan, J.A.,

793   Higurashi, A., Naka-jima, T.: Tropospheric aerosol optical thickness from the GOCART

794   model and comparisons with satellite and Sun photometer measurements. J. Atmos.

795   Sci. 59:461–483, 2002.

796   Chuang, C. C., Penner, J. E., Taylor, K. E., Grossman, A. S., and Walton, J. J.: An assessment
797   of the radiative effects of anthropogenic sulfate, J. Geophys. Res., 102, 3761–3778,
798   1997.

799   Collins, W. J., Lamarque, J.–F., Schulz, M., Boucher, O., Eyring, V., Hegglin, M. I.,
800   Maycock, A., Myhre, G., Prather, M., Shindell, D., Smith, S. J.: AerChemMIP:
801   quantifying the effects of chemistry and aerosols in CMIP6, Geosci. Model Dev., 10,
802   585–607, 2017.

803   Collins, W. D., Rasch, P. J., Boville, B. A., Hack, J. J., McCaa, J. R., Williamson, D. L,.
804   Kiehl, J. T., Briegleb, B. P., Bitz, C., Lin, S.-J., Zhang, M., and Dai, Y.: Description of
805   the NCAR Community Atmosphere Model (CAM3). Nat. Cent. for Atmos. Res.,
806   Boulder, Colo., 2004.

807   Cooke, W.F., Wilson, J.J.N.: A global black carbon aerosol model. J. Geophys. Res. Atmos.
808   101, 19395–19409, 1996.

809   Cunnold, D., Alyea, F., Phillips, N., Prinn, R.: A three-dimensional dynamical-chemical
810   model of atmospheric ozone, J. Atmos. Sci., 32, 170-194, 1975.

811   Dentener, F., Kinne, S., Bond, T., Boucher, O., Cofala, J., Generoso, S., Ginoux, P., Gong, S.,
812   Hoelzemann, J. J., Ito, A., Marelli, L., Penner, J. E., Putaud, J.-P., Textor, C., Schulz, M.,
813   van der Werf, G. R., and Wilson, J.: Emissions of primary aerosol and precursor gases in
814   the years 2000 and 1750 prescribed data-sets for AeroCom, Atmos. Chem. Phys., 6,
815   4321–4344, doi:10.5194/acp-6-4321-2006, 2006.

816   Eyring, V., Bony, S., Meehl, G. A., Senior, C. A., Stevens, B., Stouffer, R. J., and Taylor, K.
817   E.: Overview of the Coupled Model Intercomparison Project Phase 6 (CMIP6)
818   experimental design and organization, Geosci. Model Dev., 9, 1937–1958,
819   doi:10.5194/gmd-9-1937-2016, 2016.

820   Feichter, J., Kjellstrom, E., Rodhe, H., Dentener, F., Lelieveldi, J., Roelofs, G.-J.: Simulation
821   of the tropospheric sulfur cycle in a global climate model, 30: 1693-1707, 1996.

822   Feng, L., Smith, S. J., Braun, C., Crippa, M., Gidden, M. J., Hoesly, R., Klimont, Z., van
823   Marle, M., van den Berg, M., and van der Werf, G. R.: Gridded Emissions for CMIP6,
824   Geosci. Model Dev. Discuss., https://doi.org/10.5194/gmd-2019-195, 2019

825   Ghan, S. J. and Easter, R. C.: Impact of cloud-borne aerosol representation on aerosol direct
826   and indirect effects, Atmos. Chem. Phys., 6, 4163–4174, 2006.

827 Ginoux, P., M. Chin, I. Tegen, J. M. Prospero, B. Holben, O. Dubovik, and S.-J. Lin (2001),

828   Sources and distributions of dust aerosols simulated with the GOCART model, J.

829   Geophys. Res., 106, 20,255 – 20,274.

830 Giorgi, F., and Chameides, W. L.: The rainout parameterization in a photochemical model, J.

831   Geophys. Res., 90, 7872–7880, 1985.

832 Guenther, A. B., Jiang, X., Heald, C. L., et al.: The Model of Emissions of Gases and

833   Aerosols from Nature Version 2.1 (MEGAN2.1): An Extended and Updated Framework

834   for Modeling Biogenic Emissions. Geoscientific Model Development 5(6): 1471–1492,

835   2012.

836 Guenther, A., Baugh, B. Brasseur, G., Greenberg, J., Harley, P., Klinger, L,. Serca, D., and

837   Vierling, L.: Isoprene emission estimates and uncertainties for the Central African

838   EXPRESSO study domain, J. Geophys. Res., 104(D23), 30, 625–630, 639, 1999.

839 Hess, M., Koepke, P., Schult, I.: Optical properties of aerosols and clouds: the software

840   package OPAC, Bull. Am. Meteorol. Soc., 79, 831–844, 1998.

841 Hoesly, R. M., Smith, S. ., Feng, L., Klimont, Z., Janssens-Maenhout, G., Pitkanen, T.,

842   Seibert, J. J., Vu, L., Andres, R. J., Bolt, R. M., Bond, T. C., Dawidowski, L., Kholod, N.,

843   Kurokawa, J., Li, M., Liu, L., Lu, Z., Moura, M. C. P., O'Rourke, R. R., and Zhang Q.:

844   Historical (1750–2014) anthropogenic emissions of reactive gases and aerosols from the

845   Community Emission Data System (CEDS), Geosci. Model Dev., 11, 369-408, 2018

846 Horowitz, L.W., Walters, S., Mauzerall, D. L., Emmons, L. K., Rasch, P. J., Granier, C., Tie,

847   X., Lamarque, J.-F., Schultz, M. G., Tyndall, G. S., Orlando, J. J., Brasseur, G. P.: A

848   global simulation of tropospheric ozone and related tracers: Description and evaluation

849   of MOZART, version 2, J. Geophys. Res., 108(D24), 4784, doi:10.1029/2002JD002853,

850   2003.

851 Horowitz, L. W.: Past, present, and future concentrations of tropospheric ozone and aerosols:

852   Methodology, ozone evaluation, and sensitivity to aerosol wet removal, J. Geophys. Res.,

853   111, D22211, doi:10.1029/2005JD006937, 2006.

854 Hoffman, F. M., Randerson, J. T., Arora, V. K., Bao, Q., Cadule, P., Ji, D.,   Jones, C. D.,

855   Kawamiya, M., Khatiwala, S., Lindsay, K., Obata, A., Shevliakova, E., Six, K. D.,

856   Tjiputra, J. F., Volodin, E. M., and Wu, T.: Causes and implications of persistent

857   atmospheric carbon dioxide biases in Earth System Models, J. Geophys. Res. Biogeosci.,

858   119, 141–162, doi:10.1002/2013JG002381, 2014.

859 Holtslag, A. A. M., and Boville, B. A.: Local versus nonlocal boundary-layer diffusion in a
860   global climate model, J. Climate, 6, 1825–1842, 1993.

861 Hurtt, G.C., Chini, L.P., Frolking, S. et al.: Harmonization of land-use scenarios for the period
862   1500–2100: 600 years of global gridded annual land-use transitions, wood harvest, and
863   resulting secondary lands, Climatic Change, 109, 117-161, 2011.

864 Hurtt, G., et al.: input4MIPs.UofMD.landState.CMIP.UofMD-landState-2-1-h, version
865   20170126, Earth Syst. Grid Fed., http://doi.org/10.22033/ESGF/input4MIPs.1127, 2017.

866 Jacobson, M.Z.: Investigating cloud absorption effects: global absorption properties of black
867   carbon, tar balls, and soil dust in clouds and aerosols. J. Geophys. Res. 117, D06205,
868   2012.

869 Jones, C.D., Arora, V., Friedlingstein, P., Bopp, L., Brovkin, V., Dunne, J., Graven, H.,
870   Hoffman, F., Ilyina, T., John, J. G., Jung, M., Kawamiya, M., Koven, C., Pongratz, J.,
871   Raddatz, T., Randerson, J. T., and Zaehle, S.: C4MIP – The Coupled Climate–Carbon
872   Cycle Model Intercomparison Project: experimental protocol for CMIP6, Geosci. Model
873   Dev., 9, 2853–2880, doi:10.5194/gmd-9-2853-2016, 2016.

874 Lamarque, J.-F., Shindell, D. T., Josse, B., Young, P. J., Cionni, I, Eyring, V., Bergmann, D.,
875   Cameron-Smith, P., Collins,W. J., Doherty, R., Dalsoren, S., Faluvegi, G., Folberth, G.,
876   Ghan, S. J., Horowitz, L. W., Lee, Y. H., MacKenzie, I. A., Nagashima, T., Naik, V.,
877   Plummer, D., Righi, M., Rumbold, S. T., Schulz, M., Skeie, R. B., Stevenson, D. S.,
878   Strode, S., Sudo, K., Szopa, S.,Voulgarakis, A., and Zeng, G.: The Atmospheric
879   Chemistry and Climate Model Intercomparison Project (ACCMIP): overview and
880   description of models, simulations and climate diagnostics, Geosci. Model Dev., 6, 179–
881   206, doi:10.5194/gmd-6-179-2013, 2013.

882 Lamarque, J.-F., Emmons, L. K., Hess, P. G., Kinnison, D. E., Tilmes, S., Vitt, F., Heald, C.
883   L., Holland, E. A., Lauritzen, P. H., Neu, J., Orlando, J. J., Rasch, P. J., and Tyndall, G.
884   K.: CAM-chem: description and evaluation of interactive atmospheric chemistry in the
885   Community Earth System Model, Geosci. Model Dev., 5, 369–411, 2012

886 Lamarque, J.-F., Bond, T. C., Eyring, V., Granier, C., Heil, A., Klimont, Z., Lee, D., Liousse,
887   C., Mieville, A., Owen, B., Schultz, M. G., Shindell, D., Smith, S. J., Stehfest, E., Van
888   Aardenne, J., Cooper, O. R., Kainuma, M., Mahowald, N., McConnell, J. R., Naik, V.,
889   Riahi, K., and van Vuuren, D. P.: Historical (1850–2000) gridded anthropogenic and
890   biomass burning emissions of reactive gases and aerosols: methodology and application,

891   Atmos. Chem. Phys., 10, 7017-7039, https://doi.org/10.5194/acp-10-7017-2010, 2010.

892 Lawrence, D. M., Hurtt, G. C., Arneth, A., Brovkin, V., Calvin, K. V., Jones, A. D., Jones, C.

893   D., Lawrence, P. J., de Noblet-Ducoudré, N., Pongratz, J., Seneviratne, S. I., and

894   Shevliakova, E.: The Land Use Model Intercomparison Project (LUMIP) contribution to

895   CMIP6: rationale and experimental design, Geosci. Model Dev., 9, 2973–2998,

896   https://doi.org/10.5194/gmd-9-2973-2016, 2016.

897 Lohmann, U., Feichter, J., Penner, J. E., and Leaitch, W. R.: Indirect effect of sulfate and

898   carbonaceous aerosols: A mechanistic treatment. J. Geophys. Res, 105, 12193–12206,

899   2000

900 Li, W., Zhang, Y., Shi, X., Zhou, W., Huang, A., Mu, M., Qiu, B., JI, J.: Development of the

901   Land Surface Model BCC_AVIM2.0 and Its Preliminary Performance in

902   LS3MIP/CMIP6, J. Meteor. Res., 33, 851-869, doi: 10.1007/s13351-019-9016-y, 2019.

903 Liu, X. H., Penner, J. E., and Herzog, M.: Global modeling of aerosol dynamics: Model

904   description, evaluation, and interactions between sulfate and nonsulfate aerosols, J.

905   Geophys. Res.-Atmos., 110, D18206, doi:10.1029/2004jd005674, 2005.

906 Liu, X., Easter, R.C. Ghan, S.J., Zaveri, R., Rasch, P., Shi, X., Lamarque, J.-F., Gettelman, A.,

907   Morrison, H., Vitt, F., Conley, A., Park, S., Neale, R., Hannay, C., Ekman, A.M., Hess,

908   P., Mahowald, N., Collins, W., Iacono, M.J., Bretherton, C.S., Flanner, M.G., and

909   Mitchell, D.: Toward a Minimal Representation of Aerosols in Climate Models:

910   Description and Evaluation in the Community Atmosphere Model CAM5.

911   Geos.Model.Dev. 5(3):709-739. 2012.

912 Liu, X., Ma, P. -L., Wang, H., Tilmes, S., Singh, B., Easter, R. C., Ghan, S. J., and Rasch, P.

913   J.: Description and evaluation of a new four-mode version of the Modal Aerosol Module

914   (MAM4) within version 5.3 of the Community Atmosphere Model, Geosci. Model Dev.,

915   9, 505–522, https://doi.org/10.5194/gmd-9-505-2016, 2016.

916 Liu, J., Mauzerall, D.L., Horowitz, L.W., Ginoux, P., Fiore, A.M.: Evaluation intercontinental

917   transport of fine aerosols: (1) methodology, global aerosol distribution and optical depth.

918   Atmos Environ 43:4327–4338, 2009.

919 Lu, X., Zhang, L., Wu, T., Long, M., Wang, J., Jacob, D., Zhang F., Zhang, J., Eastham, S.,

920   Hu, L., Zhu, L., Liu, X., an Wei, M.: Development of the global atmospheric general

921   circulation-chemistry model BCC-GEOS-Chem v1.0: model description and evaluation,

922   submitted to Geos.Model.Dev.

923   Mahowald, N., Lamarque, J.-F., Tie, X., and Wolff, E.: Sea salt aerosol response to climate

924   change: last glacial maximum, preindustrial and doubled carbon dioxide climates, J.

925   Geophys. Res., 111, D05303, doi:10.1029/2005JD006459, 2006.

926   Martin, R. V., et al.: Interpretation of TOMS observations of tropical tropospheric ozone with

927   a global model and in situ observations, J. Geophys. Res., 107(D18), 4351,

928   doi:10.1029/2001JD001480, 2002.

929   Matsui, H., and Mahowald, N.: Development of a global aerosol model using a

930   two-dimensional sectional method: 2. Evaluation and sensitivity simulations, J. Adv.

931   Model. Earth Syst., 9, 1887–1920, doi:10.1002/2017MS000937, 2017.

932   Matthes, K., Funke, B., Andersson, M. E., Barnard, L., Beer, J., Charbonneau, P., Clilverd, M.

933   A., Dudok de Wit, T., Haberreiter, M., Hendry, A., Jackman, C. H., Kretzschmar, M.,

934   Kruschke, T., Kunze, M., Langematz, U., Marsh, D. R., Maycock, A. C., Misios, S.,

935   Rodger, C. J., Scaife, A. A., Seppälä, A., Shangguan, M., Sinnhuber, M., Tourpali, K.,

936   Usoskin, I., van de Kamp, M., Verronen, P. T., and Versick, S.: Solar forcing for CMIP6

937   (v3.2), Geosci. Model Dev., 10, 2247–2302, https://doi.org/10.5194/gmd-10-2247-2017,

938   2017.

939   Meinshausen, M., Vogel, E., Nauels, A., Lorbacher, K., Meinshausen, N., Etheridge, D. M.,

940   Fraser, P. J., Montzka, S. A., Rayner, P. J., Trudinger, C. M., Krummel, P. B., Beyerle,

941   U., Canadell, J. G., Daniel, J. S., Enting, I. G., Law, R. M., Lunder, C. R., O'Doherty, S.,

942   Prinn, R. G., Reimann, S., Rubino, M., Velders, G. J. M., Vollmer, M. K., Wang, R. H. J.,

943   and Weiss, R.: Historical greenhouse gas concentrations for climate modelling (CMIP6),

944   Geosci. Model Dev., 10, 2057–2116, https://doi.org/10.5194/gmd-10-2057-2017, 2017.

945   Mora, C., Wei, C.-L., Rollo, A., Amaro, T., Baco, A.R., Billett, D., Bopp, L., Chen, Q.,

946   Collier, M., Danovaro, R., Gooday, A.J., Grupe, B.M., Halloran, P.R., Ingels, J., Jones,

947   D.O.B., Levin, L.A., Nakano, H., Norling, K., Ramirez-Llodra, E., Rex, M., Ruh, H.A.,

948   Smith, C.R., Sweetman, A.K., Thurber, A.R., Tjiputra, J. F., Usseglio, P., Watling, L.,

949   Wu, T., Yasuhara, M.: Biotic and human vulnerability to projected ocean

950   biogeochemistry change over the 21st century, PLoS Biol 11(10): e1001682.

951   doi:10.1371/journal.pbio.1001682, 2013.

952   NCAR Command Language (Version 6.6.2) [Software], Boulder, Colorado:

953   UCAR/NCAR/CISL/TDD. http://dx.doi.org/10.5065/D6WD3XH5, 2019.

954   Neale, R. B., et al.: Description of the NCAR Community Atmosphere Model (CAM 4.0),

NCAR Tech. Note, TN-485, pp. 212, Natl. Cent. for Atmos. Res., Boulder, Colo., 2010

Neu, J. L. and Prather, M. J.: Toward a more physical representation of precipitation scavenging in global chemistry models: cloud overlap and ice physics and their impact on tropospheric ozone, Atmos. Chem. Phys. Discuss., 11, 24413–24466, doi:10.5194/acpd-11-24413-2011, 2011.

Olivier, J.G.J., Bouwman, A.F., Van der Maas, C.W.M., Berdowski, J.J.M., Veldt, C., Bloos, J.P.J., Visschedijk, A.J.H., Zandveld, P.Y.J., Haverslag, J.L., Description of EDGAR Version 2.0: A set of global emission inventories of greenhouse gases and ozone depleting substances for all anthropogenic and most natural sources on a per country basis and on $1°$ x1 $°$ grid. RIVM Techn. Report nr. 771060002, TNO-MEP report nr. R96/119.Nat. Inst. Of Public Health and the Environment/ Netherlands Organisation for Applied Scientific Research, Bilthoven, 1996.

Peng, Y., and Lohmann, U.: Sensitivity study of the spectral dispersion of the cloud droplet size distribution on the indirect aerosol effect, Geophys. Res. Lett., 30(10), 1507, doi:10.1029/2003GL017192, 2003.

Price, C., and Rind, D.: A simple lightning parameterization for calculating global lightning distributions, J. Geophys. Res., 97, 9919-9933, 1992.

Quaas, J., Boucher, O., and Lohmann, U.: Constraining the total aerosol indirect effect in the LMDZ and ECHAM4 GCMs using MODIS satellite data. Atmos Chem Phys 6,947–955, 2006.

Sander, S., Friedl, R. R., Ravishankara, A. R., et al.: Chemical Kinetics and Photochemical Data for Use in Atmospheric Studies, Evaluation Number 14, JPL Publication 02-25, NASA, Jet Propulsion Laboratory, California Institute of Technology, Pasadena, CA, 2003.

Schlesinger, M. E., Mintz, Y.: Numerical simulation of ozone production, transport and distribution with a global atmospheric general circulation model, J.Atmos.Sci., 36: 1325-1361, 1979.

Shindell, D.T., Horowitz, L.W., Schwarzkopf, M.D.: Composition Models in Climate Projections Based on Emissions Scenarios for Long-Lived and Short-Lived Radiatively Active Gases and Aerosols. H.Levy II, D.T. Shindell, A.Gilliland, M.D.Schwarzkopf, L.W.Horowitz, (eds.) .A Report by the U.S.Climate Change Science Program and the

986   Subcommittee on Global Change Research, Washington, D.C., 2008

987 Solomon, S.: Stratospheric ozone depletion: A review of concepts and history, Reviews of
988   Geophysics, 37, 275–316, 1999.

989 Taylor, K.E., Stouffer, R. J., Meehl, G. A.: An overview of CMIP5 and the experiment design,
990   Bull. Am. Meteorol. Soc. 93, 485-498, 2012.

991 Tegen, I., Neubauer, D., Ferrachat, S., Siegenthaler-Le Drian, C., Bey, I., Schutgens, N., Stier,
992   P., Watson-Parris, D., Stanelle, T., Schmidt, H., Rast, S., Kokkola, H., Schultz, M.,
993   Schroeder, S., Daskalakis, N., Barthel, S., Heinold, B., and Lohmann, U.: The global
994   aerosol–climate model ECHAM6.3–HAM2.3 – Part 1: Aerosol evaluation, Geosci.
995   Model Dev., 12, 1643–1677, https://doi.org/10.5194/gmd-12-1643-2019, 2019.

996 Textor, C., Schulz, M., Guibert, S., Kinne, S., Balkanski, Y., Bauer, S., Berntsen, T., Berglen,
997   T., Boucher, O., Chin, M., Dentener, F., Diehl, T., Easter, R., Feichter, H., Fillmore, D.,
998   Ghan, S., Ginoux, P., Gong, S., Grini, A., Hendricks, J., Horowitz, L., Huang, P., Isaksen,
999   I., Iversen, I., Kloster, S., Koch, D., Kirkevåg, A., Kristjansson, J. E., Krol, M., Lauer, A.,
1000   Lamarque, J. F., Liu, X., Montanaro, V., Myhre, G., Penner, J., Pitari, G., Reddy, S.,
1001   Seland, Ø., Stier, P., Takemura, T., and Tie, X.: Analysis and quantification of the
1002   diversities of aerosol life cycles within AeroCom, Atmos. Chem. Phys., 6, 1777–1813,
1003   https://doi.org/10.5194/acp-6-1777-2006, 2006.

1004 Thomason, L. W., Ernest, N., Millán, L., Rieger, L., Bourassa, A., Vernier, J. P., Manney, G.,
1005   Luo, B.P., Arfeuille, F., Peter, T.: A global space‐based stratospheric aerosol
1006   climatology: 1979-2016. Earth System Science Data, 10(1), 469–492, doi:
1007   10.5194/essd-10-469-2018, 2018.

1008 Tie, X., Brasseur, G., Emmons, L., Horowitz, L., and Kinnison, D.: Effects of aerosols on
1009   tropospheric oxidants: A global model study, J. Geophys. Res., 106, 2931– 2964, 2001.

1010 Tie, X., Madronich, S., Walters, S., Edwards, D., Ginoux, P., Mahowald, N., Zhang, R., Luo,
1011   C., and Brasseur, G.: Assessment of the global impact of aerosols on tropospheric
1012   oxidants, J. Geophys. Res., 110, D03204, doi:10.1029/2004JD005359, 2005.

1013 Tilmes, S., Lamarque, J.-F., Emmons, L. K., Kinnison, D. E., Marsh, D., Garcia, R. R., Smith,
1014   A. K., Neely, R. R., Conley, A., Vitt, F., Val Martin, M., Tanimoto, H., Simpson, I.,
1015   Blake, D. R., and Blake, N.: Representation of the Community Earth System Model
1016   (CESM1) CAM4-chem within the Chemistry-Climate Model Initiative (CCMI),
1017   Geoscientific Model Development, 9, 1853-1890, 2016.

1018 Todd-Brown, K.E.O., Randerson, J.T., Hopkins, F., Arora, V., Hajima, T., Jones, C.,

1019   Shevliakova, E., Tjiputra, J., Volodin, E., Wu, T., Zhang, Q., Allison, S.D.: Changes in

1020   soil organic carbon storage predicted by Earth system models during the 21st century,

1021   Biogeosciences, 11, 2341-2356, 2014.

1022 Van Marle, M.J.E., S. Kloster, B.I. Magi, J.R. Marlon, A.-L. Daniau, R.D. Field, A. Arneth,

1023   M. Forrest, S. Hantson, N.M. Kehrwald, W. Knorr, G. Lasslop, F. Li, S. Mangeon, C.

1024   Yue, J.W. Kaiser, and G.R. van der Werf, 2017: Historic global biomass burning

1025   emissions for CMIP6 (BB4CMIP) based on merging satellite observations with proxies

1026   and fire models (1750-2015). Geosci. Model Dev., 10, 3329-3357,

1027   doi:10.5194/gmd-10-3329-2017.

1028 Wang, J., Hoffmann, A. A., Park, R., Jacob, D. J., and Martin, S. T.: Global distribution of

1029   solid and aqueous sulfate aerosols: effect of the hysteresis of particle phase transitions, J.

1030   Geophys. Res., 113, D11206, Doi:11210.11029/12007JD009367, 2008a.

1031 Wang, J., Jacob, D. J., and Martin, S. T.: Sensitivity of sulfate direct climate forcing to the

1032   hysteresis of particle phase transitions, J. Geophys. Res., 113, D11207,

1033   doi:11210.11029/12007JD009368, 2008b.

1034 Wesely, M. L.: Parameterization of surface resistance to gaseous dry deposition in

1035   regional-scale numerical models, Atmos. Environ., 23, 1293–1304, 1989.

1036 Wild, M., Folini, D., Schar, C., Loeb, N., Dutton, E.G., Konig-Langlo, G.: The global energy

1037   balance from a surface perspective, Climate Dynamics, 40: 3107-3134, 2013.

1038 Williamson, D. L., and Rasch, P. J.: Two-dimensional semi-Lagrangian transport with

1039   shapepreserving interpolation, Mon. Wea. Rev., 117, 102–129, 1989.

1040 Wofsy, S. C. and the HIPPO team: HIAPER Pole-to-Pole Observations (HIPPO): fine-grained,

1041   global-scale measurements of climatically important atmospheric gases and aerosols,

1042   Philo T. R. Soc. A, 369, 2073–86, doi:10.1098/rsta.2010.0313, 2011.

1043 Wu, T., Song, L., Li, W., Wang, Z., Zhang, H., Xin, X., Zhang, Y., Zhang, L., Li, J., Wu, F.,

1044   Liu, Y., Zhang, F., Shi, X., Chu, M., Zhang, J., Fang, Y., Wang, F., Lu, Y., Liu, X., Wei,

1045   M., Liu, Q., Zhou, W., Dong, M., Zhao, Q., Ji, J., Li, L., Zhou, M.: An overview of BCC

1046   climate system model development and application for climate change studies. J. Meteor.

1047   Res., 28(1), 34-56, 2014.

1048 Wu, T., Li, W., Ji, J., Xin, X., Li, L., Wang, Z, Zhang, Y., Li, J., Zhang, F., Wei, M., Shi, X.,

1049   Wu, F., Zhang, L., Chu, M., Jie, W., Liu, Y., Wang, F., Liu, X., Li, Q., Dong, M., Liang,

1050   X., Gao, Y., Zhang, J.: Global carbon budgets simulated by the Beijing climate center

1051   climate system model for the last century. J Geophys Res Atmos, 118, 4326-4347. doi:

1052   10.1002/jgrd.50320, 2013.

1053   Wu, T., Lu, Y., Fang, Y., Xin, X., Li, L., Li, W., Jie, W., Zhang, J., Liu, Y., Zhang, L., Zhang,

1054   F., Zhang, Y., Wu, F., Li, J., Chu, M., Wang, Z., Shi, X., Liu, X., Wei, M., Huang, A.,

1055   Zhang, Y., and Liu, X.: The Beijing Climate Center Climate System Model (BCC-CSM):

1056   the main progress from CMIP5 to CMIP6, Geos.Model Dev., 12, 1573-1600,

1057   http://doi.org/10.5194/gmd-12-1573-2019, 2019.

1058   Wu, Tongwen, Zhang, Fang, Zhang, Jie, et al.: Model code and data for Wu et al, "Beijing

1059   Climate Center Earth System Model version 1 (BCC-ESM1): Model Description and

1060   Evaluation of Aerosol Simulations", GMD publication.

1061   http://doi.org/10.5281/zenodo.3609337, 2020.

1062   Young, P. J., Archibald, A. T., Bowman, K. W., Lamarque, J. F., Naik, V., Stevenson, D. S.,

1063   Tilmes, S., Voulgarakis, A., Wild, O., Bergmann, D., Cameron-Smith, P., Cionni, I.,

1064   Collins, W. J., Dalsøren, S. B., Doherty, R. M., Eyring, V., Faluvegi, G., Horowitz, L.

1065   W., Josse, B., Lee, Y. H., MacKenzie, I. A., Nagashima, T., Plummer, D. A., Righi, M.,

1066   Rumbold, S. T., Skeie, R. B., Shindell, D. T., Strode, S. A., Sudo, K., Szopa, S., and

1067   Zeng, G.: Pre-industrial to end 21st century projections of tropospheric ozone from the

1068   Atmospheric Chemistry and Climate Model Intercomparison Project (ACCMIP), Atmos.

1069   Chem. Phys., 13, 2063-2090, http://doi/.org/10.5194/acp-13-2063-2013, 2013.

1070   Young, P. J., Naik, V., Fiore, A. M., Gaudel, A., Guo, J., Lin, M. Y., Neu, J. L., Parrish, D. D.,

1071   Rieder, H. E., Schnell, J. L., Tilmes, S., Wild, O., Zhang, L., Ziemke, J. R., Brandt, J.,

1072   Delcloo, A., Doherty, R. M., Geels, C., Hegglin, M. I., Hu, L., Im, U., Kumar, R., Luhar,

1073   A., Murray, L., Plummer, D., Rodriguez, J., Saiz-Lopez, A., Schultz, M. G., Woodhouse,

1074   M. T., and Zeng, G.: Tropospheric Ozone Assessment Report: Assessment of

1075   global-scale model performance for global and regional ozone distributions, variability,

1076   and trends, Elem Sci Anth, 6, 10, http://doi/.org/10.1525/elementa.265, 2018.

1077   Zender, C., Bian, H., and Newman, D.: Mineral Dust Entrainment and Deposition (DEAD)

1078   model: Description and 1990s dust climatology, J. Geophys. Res., 108(D14), 4416, doi:

1079   10.1029/2002JD002775, 2003.

1080   Zhang, J., Wu, T., Shi, X., Zhang F., Li, J., Chu, M., Liu, Q., Yan, J., Ma, Q., Wei, M.: BCC

1081   BCC-ESM1 model output prepared for CMIP6 AerChemMIP. Version

1082   YYYYMMDD[1],   Earth   System   Grid   Federation,

1083   https://doi.org/10.22033/ESGF/CMIP6.1733, 2019.

1084

Table 1. Chemical species considered in BCC-AGCM3-Chem. Species marked with star (*) denote those added in BCC-ESM1 apart from the 63 species used in MOZART2. In the column of surface emission, interactive surface emissions are considered for sea salt and dust.

	Species	Dry deposition	Wet deposition	Surface emission	Aircraft emission	Volcanic emission
	O_3	√				
	N_2O			√		
	N					
	NO	√		√	√	
	NO_2	√				
	NO_3					
	HNO_3	√	√			
	HO_2NO_2	√	√			
	N_2O_5					
	CH_4	√		√	√	
	CH_3O_2					
	CH_3OOH	√	√			
	CH_2O	√	√	√		
	CO	√		√	√	
	OH					
	HO_2					
	H_2O_2	√	√			
	C_3H_6			√		
	ISOP			√		
Gas tracers	PO_2					
	CH_3CHO	√	√	√		
	POOH	√	√			
	CH_3CO_3					
	CH_3COOOH	√	√			
	PAN	√				
	ONIT	√	√			
	C_2H_6			√		
	C_2H_4			√		
	C_4H_{10}			√		
	MPAN	√				
	$ISOPO_2$					
	MVK		√			
	MACR		√			
	$MACRO_2$					
	MACROOH	√	√			
	MCO_3					
	$C_2H_5O_2$					
	C_2H_5OOH	√	√			
	$C_{10}H_{16}$			√		

Species name		Dry deposition	Wet deposition	Surface emission	Aircraft emission	Volcanic emission
	C_3H_8			√		
	$C_3H_7O_2$					
	C_3H_7OOH	√	√			
	CH_3COCH_3	√		√		
	ROOH		√			
	CH_3OH	√	√	√		
	C_2H_5OH	√	√	√		
	GLYALD	√	√			
	HYAC	√	√			
	EO_2					
	EO					
	HYDRALD	√	√			
Gas tracers	RO_2					
	CH_3COCHO	√	√	√		
	Rn-222					
	Pb-210	√	√			
	$ISOPNO_3$		√			
	ONITR	√	√			
	XO_2					
	XOOH	√	√			
	ISOPOOH	√	√			
	H_2	√		√		
	Stratospheric O_3	√				
	Inert O_3	√				
	SO_2^*	√	√	√	√	√
	DMS^*			√		
	NH_3^*			√	√	
	SO_4^{2-*}	√	√			
	$OC1^*$	√	√	√	√	
	$OC2^*$	√	√	√	√	
	$BC1^*$	√	√	√	√	
	$BC2^*$	√	√	√	√	
	$SSLT01^*$	√	√			
Aerosols	$SSLT02^*$	√	√			
	$SSLT03^*$	√	√			
	$SSLT04^*$	√	√			
	$DST01^*$	√	√			
	$DST02^*$	√	√			
	$DST03^*$	√	√			
	$DST04^*$	√	√			

1094   Table 2. Gas-phase chemical reactions for NH_3 and bulk aerosols precursors following

1095   CAM-Chem (Lamarque et al., 2012). The reaction rates (s^{-1}) refer to Tie et al. (2001) and

1096   Sander et al. (2003), and Cooke and Wilson (1996). Temperature (T) is expressed in K, air

1097   density (M) in molecule cm^{-3}, ki and ko in cm^3 $molecule^{-1}$ s^{-1}.

1098

Chemical reactions	Rate
$NH_3 + OH \rightarrow H_2O$	1.70E-12*exp(–710/T)
$SO_2 + OH \rightarrow SO_4^{2-}$	ko/(1.+ko*M/ki)*f**(1./(1.+log10(ko*M/ki)), in which
	ko=3.0E-31*(300/T)**3.3; ki=1.E-12; f =0.6
$DMS + OH \rightarrow SO_2$	9.60E-12*exp(-234./T)
$DMS + OH \rightarrow .5*SO_2 + .5*HO_2$	1.7E−42*exp(7810/T)*M*0.21/(1+5.5E−31*exp(7460/T)* M* 0.21)
$DMS + NO_3 \rightarrow SO_2 + HNO_3$	1.90E-13*exp(520/T)
$BC1 \rightarrow BC2$	7.10E-06
$OC1 \rightarrow OC2$	7.10E-06

1099
1100

1101

1102
Table 3. Size and density parameters of bulk aerosols.

1103

Aerosols	Species Name	Mean radius (μm) / bin size (μm)	Geometric standard deviation (μm)	Density (g cm^{-3})
SO$_4^{2-}$	Sulfate	0.05	2.03	1.77
BC1	hydrophobic black carbon	0.02	2.00	1.0
BC2	hydrophilic black carbon	0.02	2.00	1.0
OC1	hydrophobic organic carbon	0.03	2.24	1.8
OC2	hydrophilic organic carbon	0.03	2.24	1.8
DST01	Dust	0.55/ bin: 0.1-1.0	2.00	2.5
DST02	Dust	1.75 / bin: 1.0-2.5	2.00	2.5
DST03	Dust	3.75 / bin: 2.5-5.0	2.00	2.5
DST04	Dust	7.50 / bin: 5.0-10.	2.00	2.5
SSLT01	Sea salt	0.52 / bin: 0.2-1.0	2.00	2.2
SSLT02	Sea salt	2.38 / bin: 1.0-3.0	2.00	2.2
SSLT03	Sea salt	4.86 / bin: 3.0-10.	2.00	2.2
SSLT04	Sea salt	15.14 / bin: 10.-20.	2.00	2.2

1104

Table 4. Source of emission data. MOZART2 data denote the standard tropospheric chemistry package for MOZART contains surface emissions from the EDGAR 2.0 data base (Olivier et al., 1996). ACCMIP data are downloaded from the IPCC ACCMIP emission inventory (http://accent.aero.jussieu.fr/ACCMIP.php) and they vary from 1850 to 2000, in 10-year steps (Lamarque et al., 2010). CMIP6 data are from https://esgf-node.llnl.gov/search/input4mips/. Anthropogenic emission includes Industrial and fossil fuel use, agriculture, ships, and etc. Biomass burning includes vegetation fires incl. fuel wood and agricultural burning.

Species	Anthropogenic emission	Biomass burning	Biogenic emissions from vegetation	Biogenic emissions from soil	Oceanic emissions	Airplane emission	Volcanic emission
C_2H_4	CMIP6	CMIP6	On-line computation		MOZART2		
C_2H_5OH	CMIP6	CMIP6					
C_2H_6	CMIP6	CMIP6	ACCMIP		MOZART2		
C_3H_6	CMIP6	CMIP6	On-line computation		MOZART2		
C_3H_8	CMIP6	CMIP6	ACCMIP		MOZART2		
C_4H_{10}	CMIP6	CMIP5	MOZART2		MOZART2		
CH_2O	CMIP6	CMIP6					
CH_3CHO	ACCMIP	CMIP6					
CH_3COCHO		CMIP6					
CH_3OH	ACCMIP	CMIP6	ACCMIP				
CH_3COCH_3	ACCMIP	ACCMIP	On-line computation		MOZART2		
ISOP		CMIP5	On-line computation				
$C_{10}H_{16}$		CMIP6	On-line computation				
CH_4	CMIP6	CMIP6	MOZART2		MOZART2	CMIP6	
CO	CMIP6	CMIP6	ACCMIP	MOZART2	ACCMIP	CMIP6	
H_2	MOZART2	CMIP6		MOZART2	MOZART2		
N_2O	MOZART2	CMIP6		MOZART2	MOZART2		
NH_3	CMIP6	CMIP6		ACCMIP	ACCMIP	CMIP6	
NO	CMIP6	CMIP6		ACCMIP		CMIP6	
SO_2	CMIP6	CMIP6				CMIP6	ACCMIP
DMS					ACCMIP		
OC1	CMIP6	CMIP6				CMIP6	
OC2	CMIP6	CMIP6	On-line computation			CMIP6	
BC1	CMIP6	CMIP6				CMIP6	
BC2	CMIP6	CMIP6				CMIP6	

Table 5. Global budgets for DMS, SO_2, and sulfate in the period of 1991 to 2000. Units are sources and sinks, Tg(S) yr^{-1}; burden, Tg; lifetime, days.

		BCC-ESM (1991-2000 mean)	Other studies and CMIP5 data
DMS	Sources	27.4	
	Emission	27.4	10.7-23.7[a]
	Sinks	28.0	
	Gas-phase oxidation	28.0	
	Burden	0.12	0.04-0.29[a]
	Lifetime	0.78	0.5-3.0[a]
SO_2	Sources	76.93	
	Emission at surface	63.63	
	Emission from airplane	0.10	
	DMS oxidation	13.20	10.0-24.7[a]
	Sinks	76.96	
	Dry deposition	18.53	16.0-55.0[a]
	Wet deposition	9.36	0.0-19.9[a]
	Gas-phase oxidation	10.33	6.1-16.8[a]
	Aqueous-phase oxidation	38.74	24.5-57.8[a]
	Burden	0.48	0.40-1.22[a]
	Lifetime	1.12	0.6-2.6[a]
SO_4^{2-}	Sources	49.05	59.67$\pm$13.13[b]
	Emission	0.00	
	SO_2 aqueous-phase oxidation	38.73	
	SO_2 gas-phase oxidation	10.32	
	Sinks	49.06	
	Dry deposition	2.20	4.96-5.51[d]
	Wet deposition	46.86	39.34-40.20[d]
	Burden	1.89	1.98$\pm$0.48[b], 1.71[c], 1.2[g], 2.22-2.43[h]
	Lifetime	4.69	4.12$\pm$0.74[b], 3.72-3.77[d] 3.3[g], 3.7-4.0[h]

Notes: References denote a for Liu et al. (2005), b for Textor et al. (2006), c for the values derived from CMIP5 prescribed aerosol masses averaged from 1991 to 2000, d for Liu et al. (2012), g for Matsui and Mahowald (2017), and h for Tegen et al. (2019). Values of DMS, SO_2, and sulfate burdens in the literature d are transferred from TgS to Tg (species) for units consistence.

Table 6. Same as Table 5, but for global budgets for black carbon, organic carbon, dust, and sea salts. Units are sources and sinks, Tg yr^{-1}; burden, Tg; lifetime, days.

		BCC-ESM (1991-2000 mean)	Other studies and CMIP5 data
BC	Sources	7.22	
	Emission	7.22	11.9±2.7[b], 7.8[g]
	Sinks	7.24	7.75[d], 7.8[g]
	Dry deposition	0.90	0.27[g], 1.30-1.64[e]
	Wet deposition	6.34	7.5[g], 6.10-6.45[e]
	Burden	0.13	0.114[c], 0.24±0.1[b], 0.11[g],0.14-0.26[h], 0.084-0.123[e]
	Lifetime	6.60	7.12±2.35[b], 3.95-4.80[e], 5.0[g], 6.3-7.5[h]
OC	Sources	32.29	
	Fossil and biofuel emission	13.91	
	Natural emission	18.38	
	Sinks	32.30	
	Dry deposition	2.44	
	Wet deposition	29.86	
	Burden	0.62	0.69[c], 1.7±0.45[b],1.0-2.2[h]
	Lifetime	5.00	6.54±1.76[b], 4.56−4.90[d], 6.4[g],5.4-6.6[h]
Dust	Sources	2592.0	1840[b],2943.5−3121.9[d], 2677[g]
	Sinks	2592.0	
	Dry deposition	1630.8	1444[g]
	Wet deposition	961.2	1245[g]
	Burden	22.93	20.41[c], 22.424.7[d], 35.9[f], 19.2±7.68[b], 28.5[g], 16.5-17.9[h]
	Lifetime	3.23	4.14±1.78[b], 2.61−3.07[d], 3.9[g], 5.3-5.7[h]
Sea Salt	Sources	4667.2	4965.5-5004.1[d], 5039[g]
	Sinks	4667.4	
	Dry deposition	2978.5	2158[g]
	Wet deposition	1688.9	2918[g]
	Burden	11.89	7.58−10.37[a], 6.4±3.4[b], 11.84[c], 13.6[g], 3.9[h]
	Lifetime	0.93	0.41±0.24[b],0.55−0.76[d], 0.98[g], 1.2-1.3[h]

Notes: References denote a for Liu et al. (2005), b for Textor et al. (2006), c derived from CMIP5 prescribed aerosol masses averaged from 1991 to 2000, d for Liu et al. (2012), e for Liu et al. (2016), f for Ginoux (2001), g for Matsui and Mahowald (2017), and h for Tegen et al. (2019).
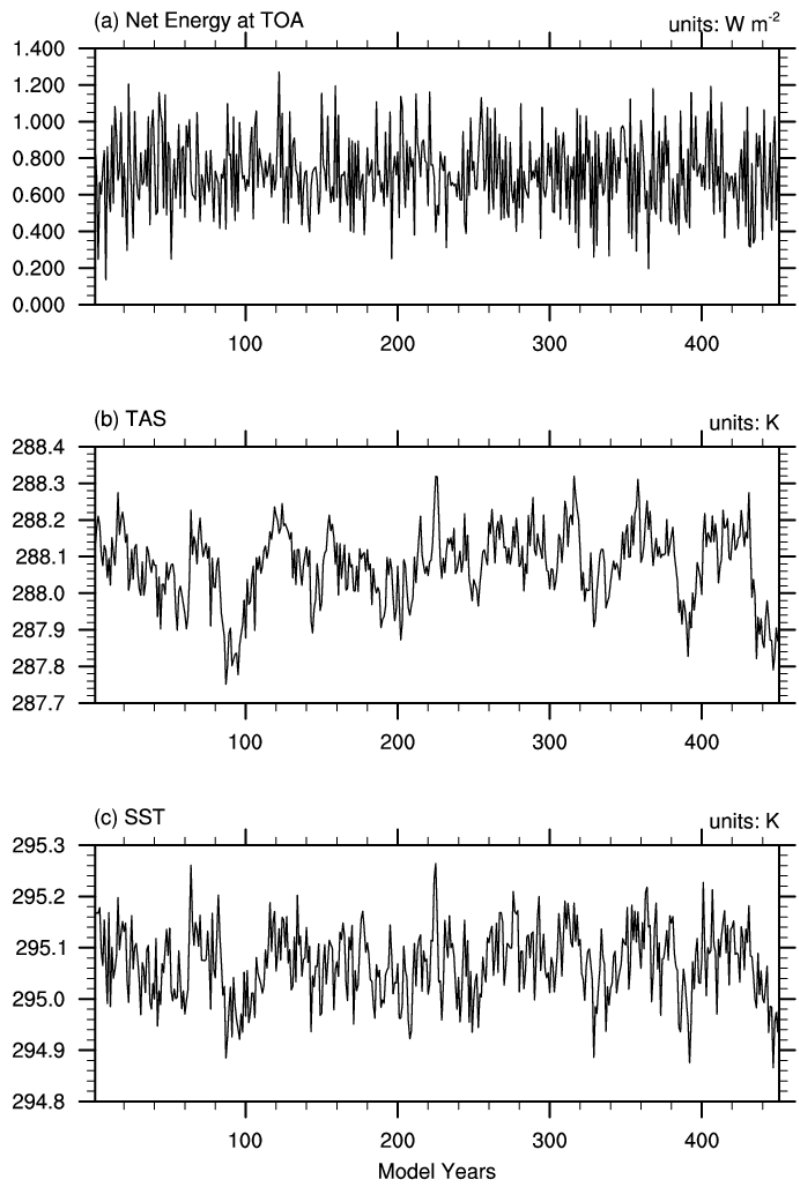
Figure 1. The time series of global and annual mean of (a) net energy budget at top of atmosphere (W m^{-2}), (b) near-surface air temperature (K), and (c) sea surface temperature (K) in the last 450 years of the piControl simulation.
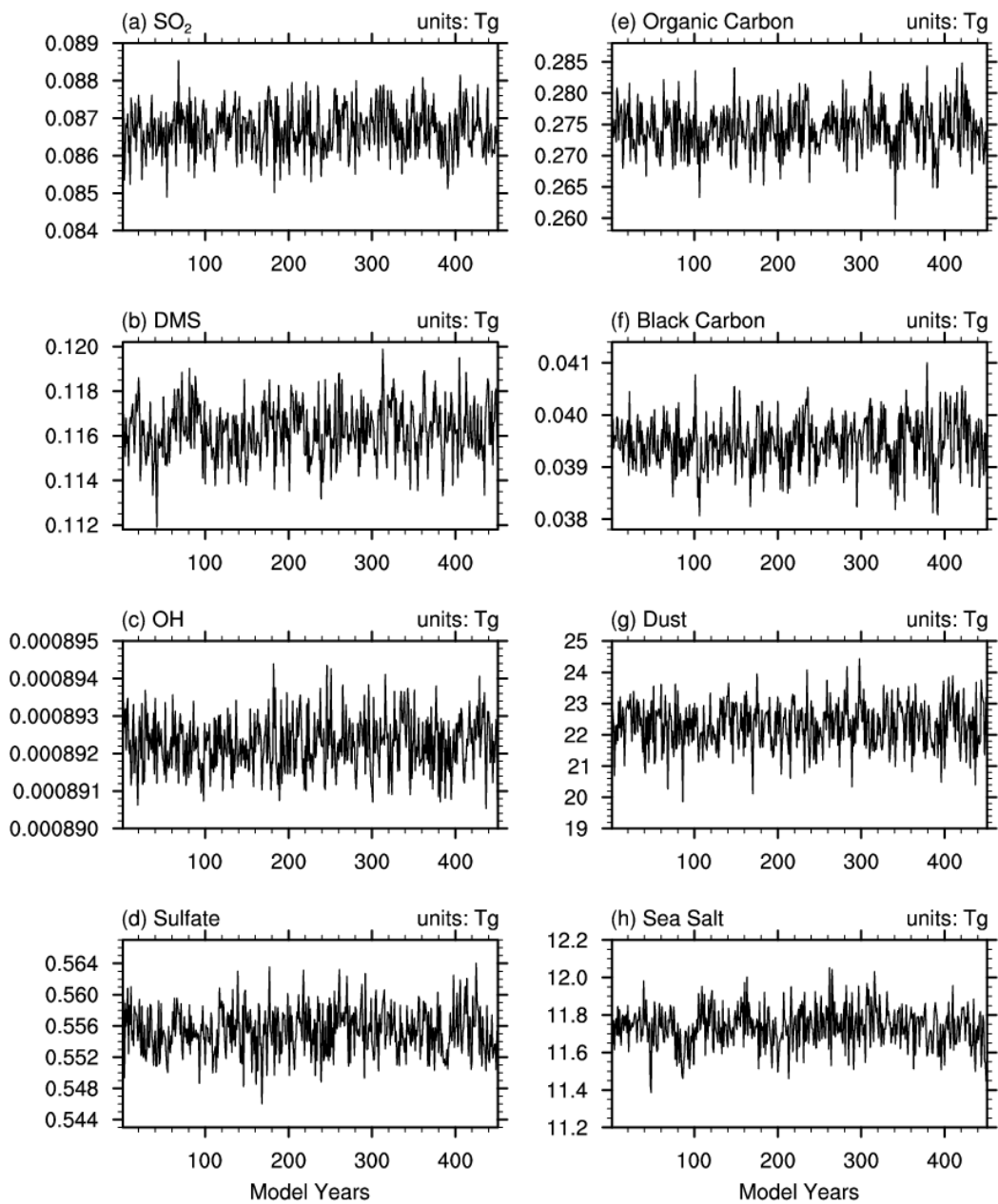
Figure 2. Same as in Figure 1, but for the global burdens of (a) SO₂, (b) DMS, (c) OH, and (d-h) different aerosols in the troposphere (below 100 hPa). Units are Tg.
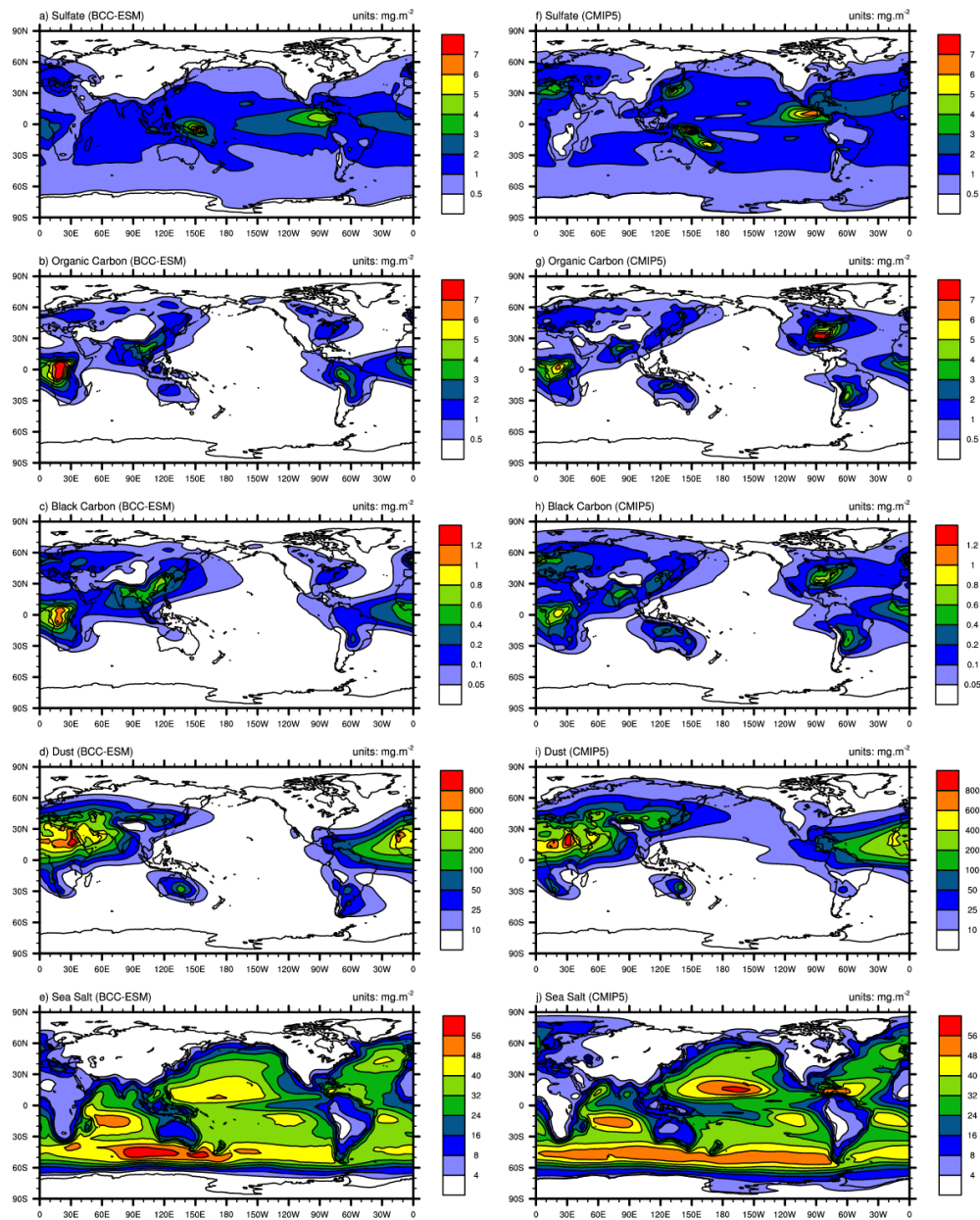
Figure 3. Global distributions of annual mean mass burdens of sulfate (SO_4^{2-}; first row), organic carbon (OC; second row), black carbon (BC; third row), dust (fourth row), and sea salt (fifth row) aerosols in the whole atmospheric column. The left panels show the mean averaged for the last 100 years of BCC-ESM pre-industrial piControl simulations, and the right panels show the CMIP5 recommended aerosol concentrations in year 1850 (the website at IIASA http://tntcat.iiasa.ac.at/RcpDb/.). Units: mg m^{-2}.
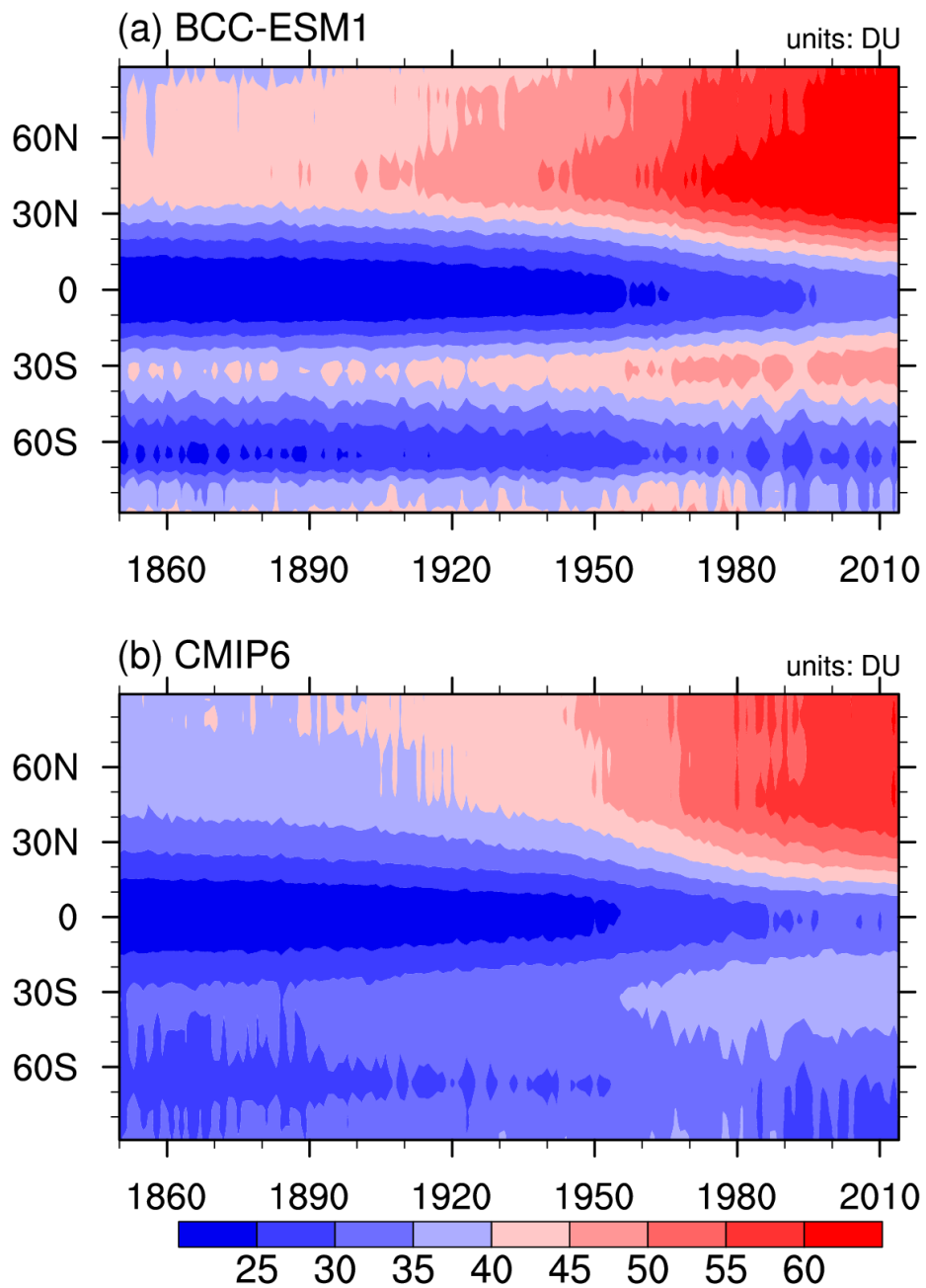
Figure 4. Zonal mean of yearly mean concentration of ozone column in the troposphere below 300 hPa to the ground from 1871 to 1999 for (a) BCC-ESM1 and (b) CMIP6 data. Unit: DU.
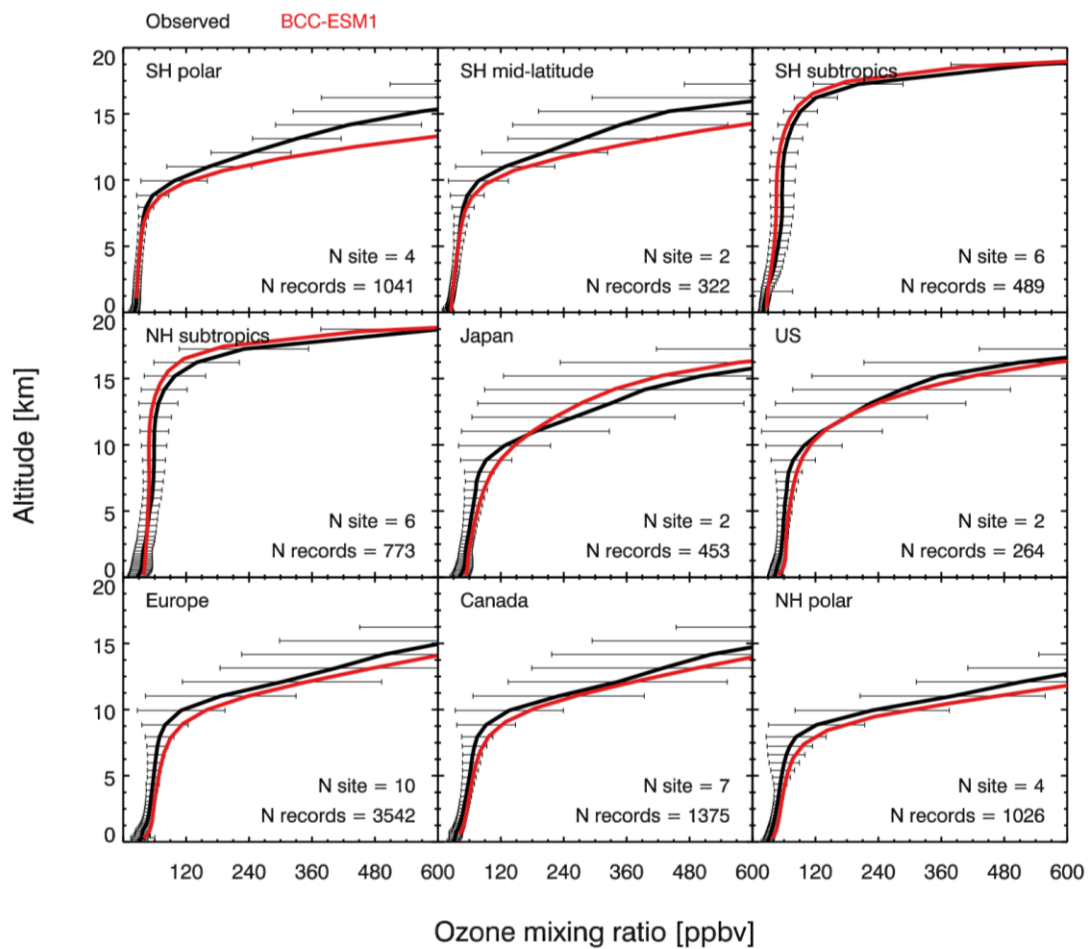
Figure 5. Vertical profiles of annual mean ozone concentrations from observations averaged for 2010-2014 in nine regions (black) and from the BCC-ESM1 simulations (red). The observations are derived from 41 global WOUDC sites.
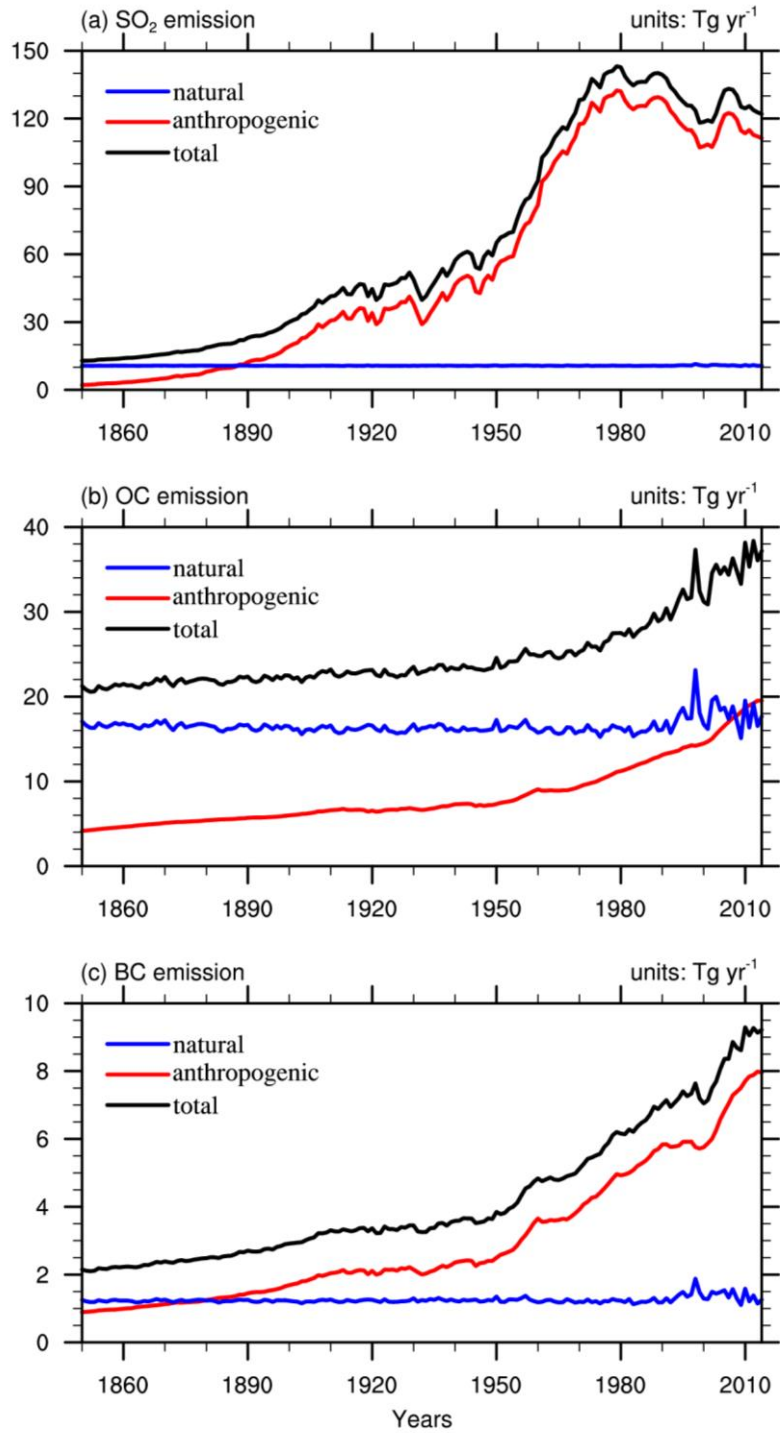
Figure 6. Global annual anthropogenic, natural, and total emissions of SO$_2$, organic carbon (OC), and black carbon (BC) in the BCC-ESM1 historical simulation. All the biomass burning emissions are included in natural emissions in (a)-(c). Units: Tg yr^{-1}.
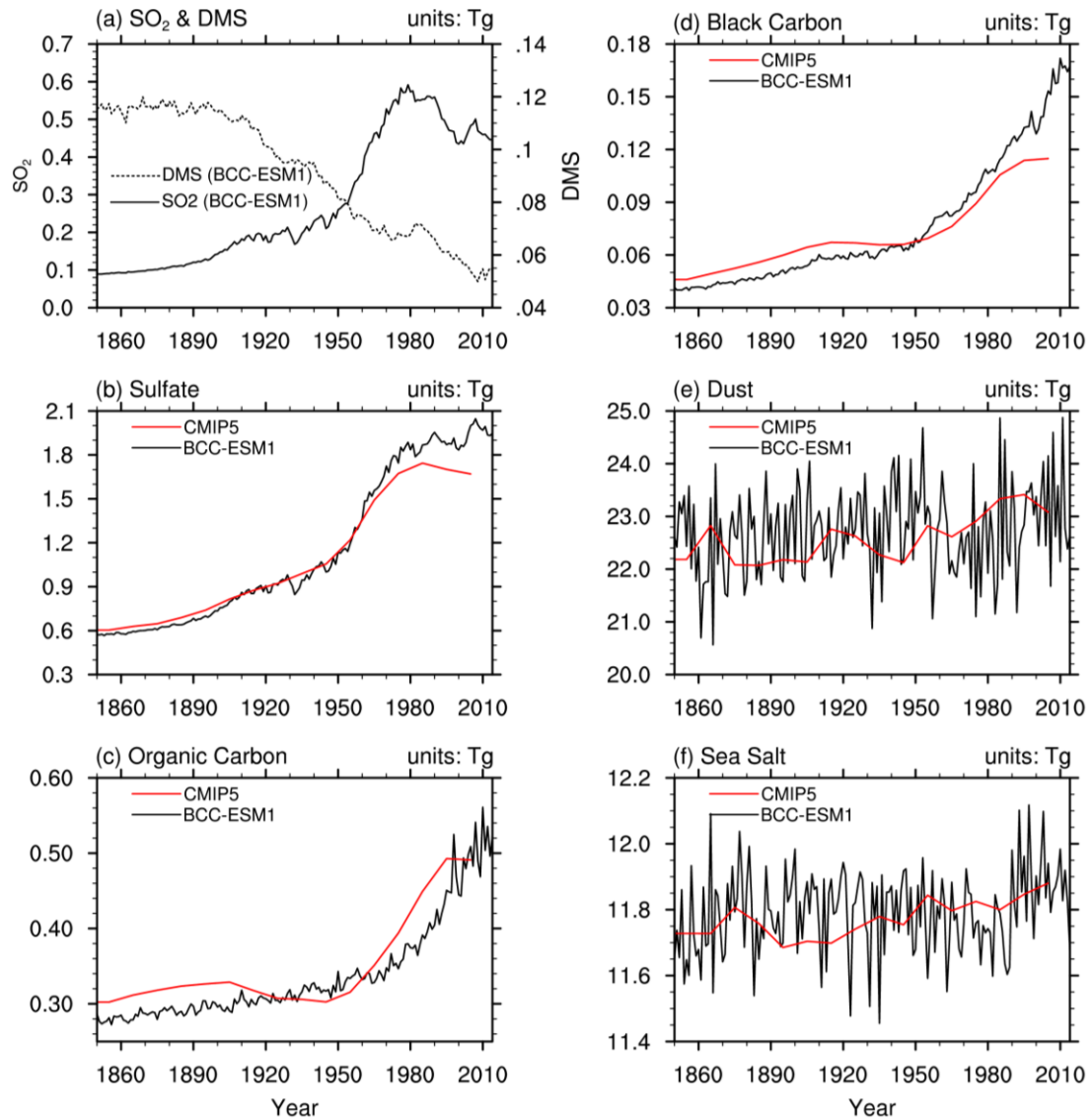
Figure 7. The time series of global yearly amounts of (a) SO₂ and DMS and (b-f) aerosols in the whole atmosphere column from the CMIP6 historical simulations of BCC-ESM1 (black lines) and the CMIP5-recommended aerosols masses (red lines). The yearly CMIP5 data are interpolated from the time series in 10-year interval. Units: Tg.
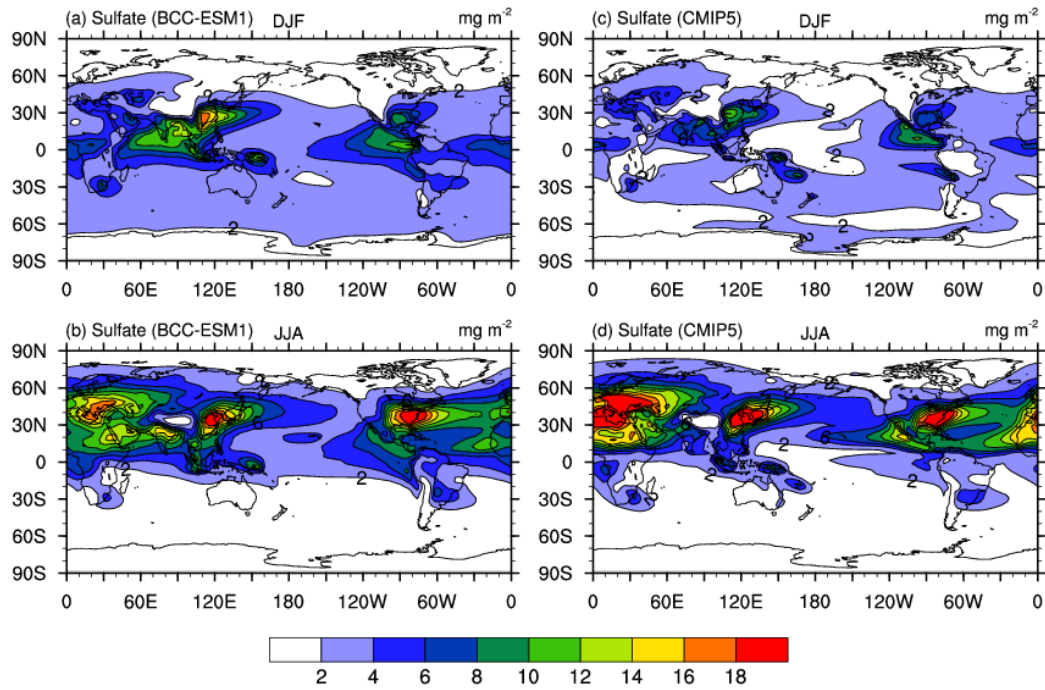
Figure 8. December-January-February (DJF; top panels) and June-July-August (JJA; bottom panels) mean sulfate (SO_4^{2-}) aerosol column mass concentrations averaged for the period of 1971-2000. Left panels show the historical simulations of BCC-ESM1, and right panels the CMIP5-recommended data. Units: mg.m^{-2}.
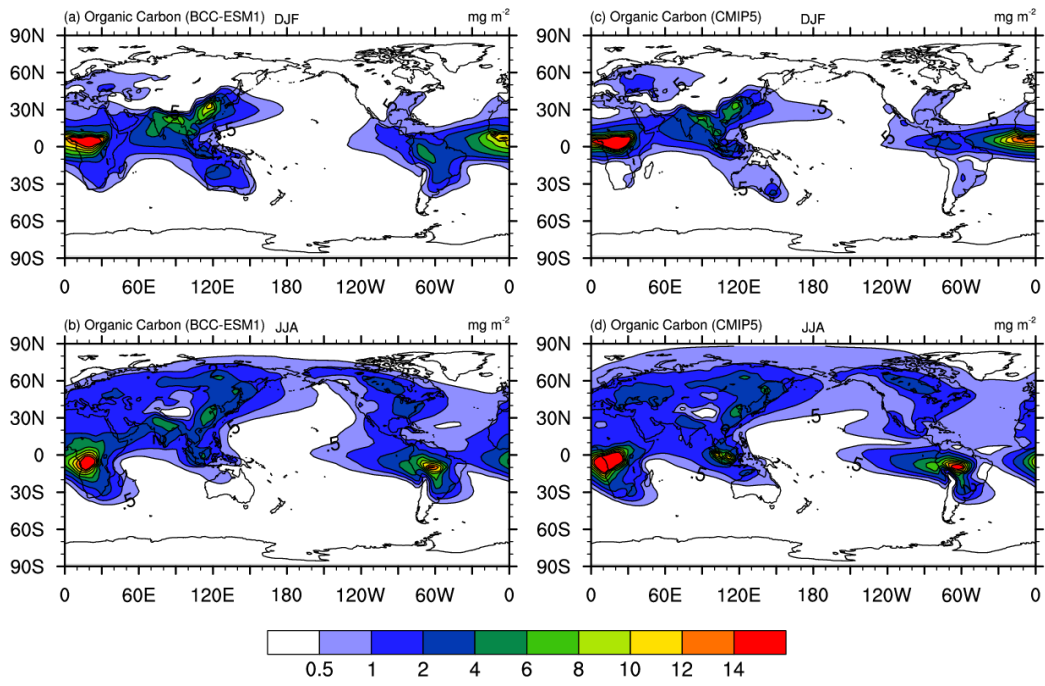
Figure 9. The same as in Figure 8, but for organic carbon (OC) aerosol column mass concentrations. Units: mg m^{-2}.
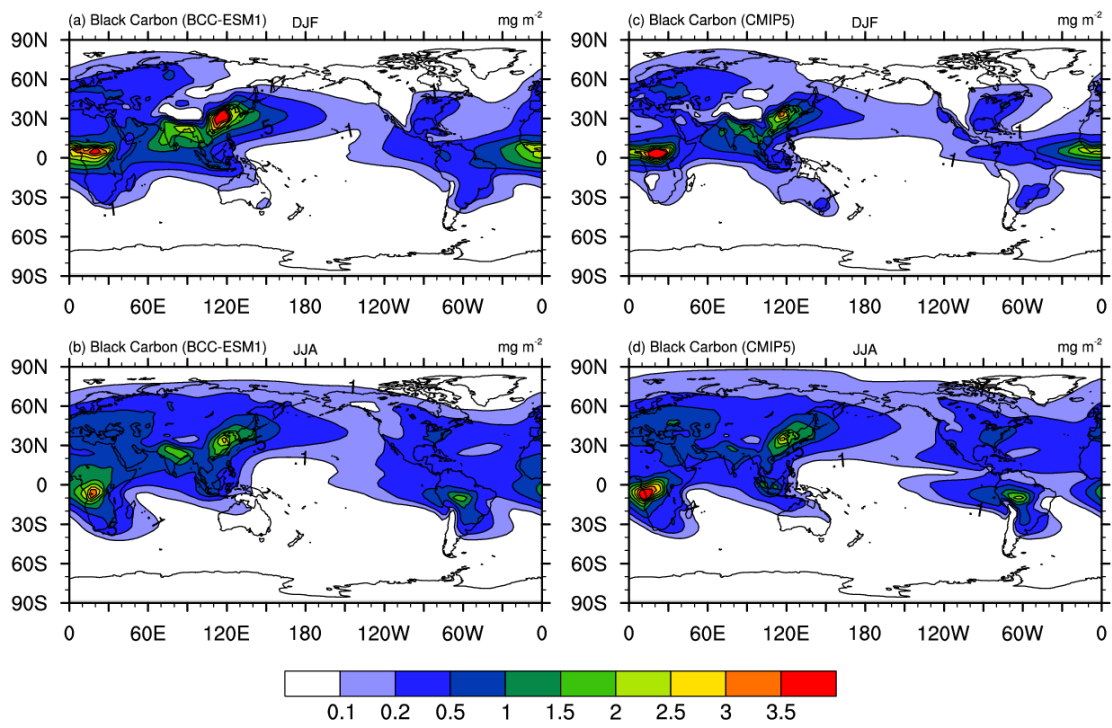
Figure 10. The same as in Figure 8, but for black carbon (BC) aerosol. Units: mg.m^{-2}.
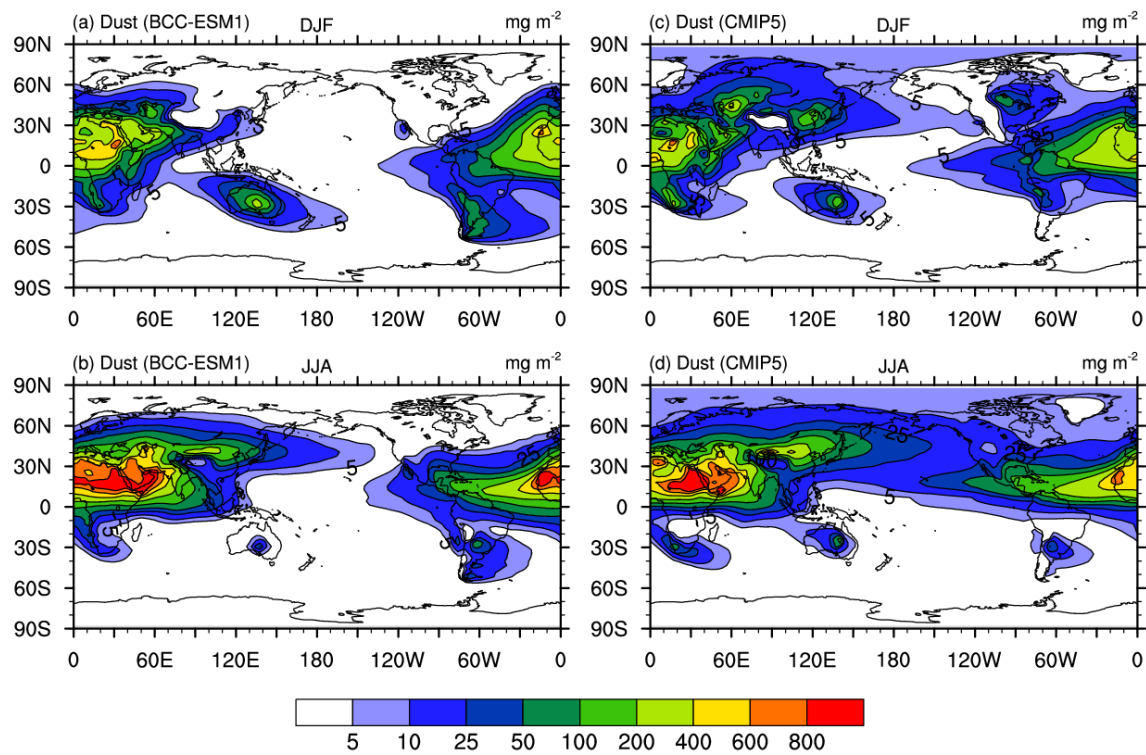
Figure 11. The same as in Figure 8, but for dust aerosol. Units: mg.m^{-2}.
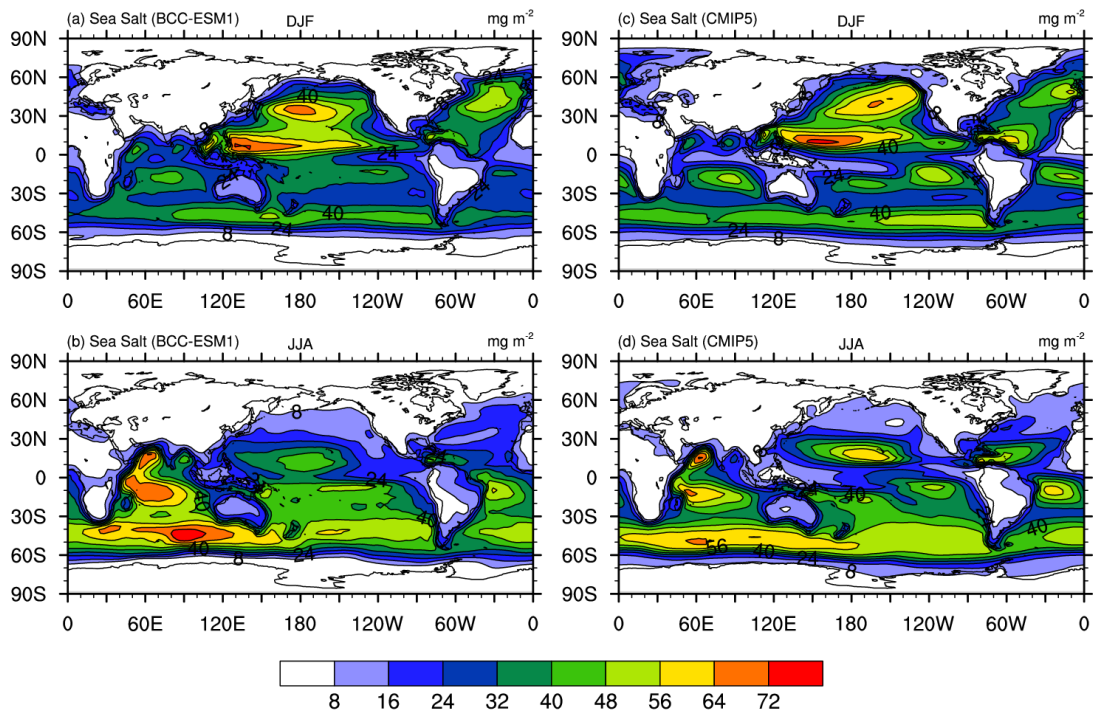
Figure 12. The same as in Figure 8, but for sea salt (SSLT) aerosol. Units: mg.m^{-2}.
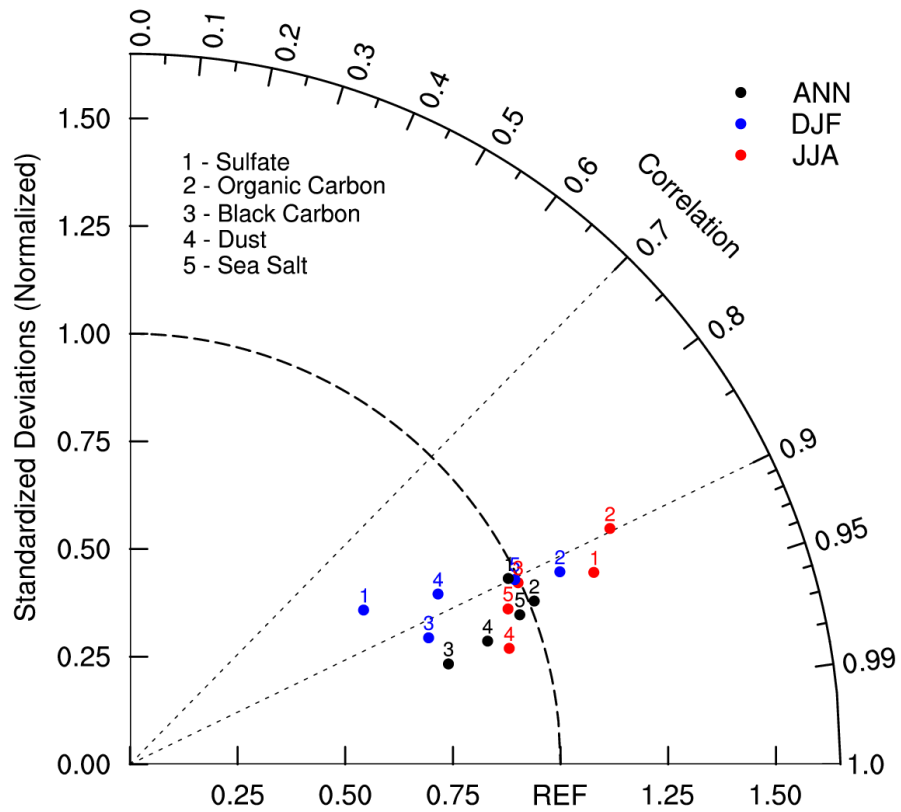
Figure 13. Taylor diagram for the global aerosols climatology (1971–2000) of sulfate, organic carbon, black carbon, dust, and sea salt averaged for December-January-February (DJF), June-July-August (JJA), and annual respectively. The radial coordinate shows the standard deviation of the spatial pattern, normalized by the observed standard deviation. The azimuthal variable shows the correlation of the modelled spatial pattern with the observed spatial pattern. Analysis is for the whole globe. The reference dataset is CMIP5-prescribed dataset.
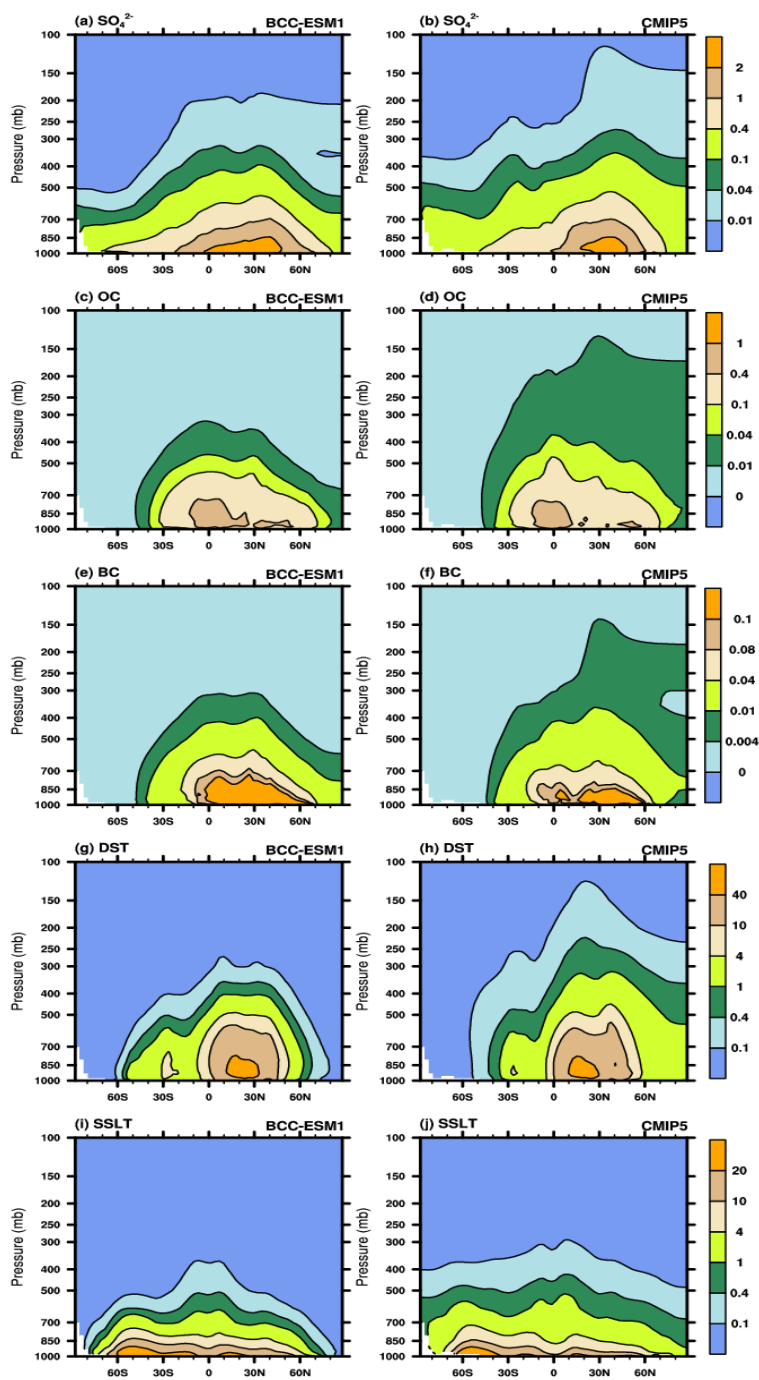
Figure 14. Latitude-pressure distributions of zonally-averaged annual mean sulfate, organic carbon, black carbon, dust, and sea salt aerosol concentrations for the period of 1971-2000. Left panels show the   CMIP6 historical simulation of BCC-ESM1, and right panels the CMIP5 recommendation data. Units: μg m^{-3}.
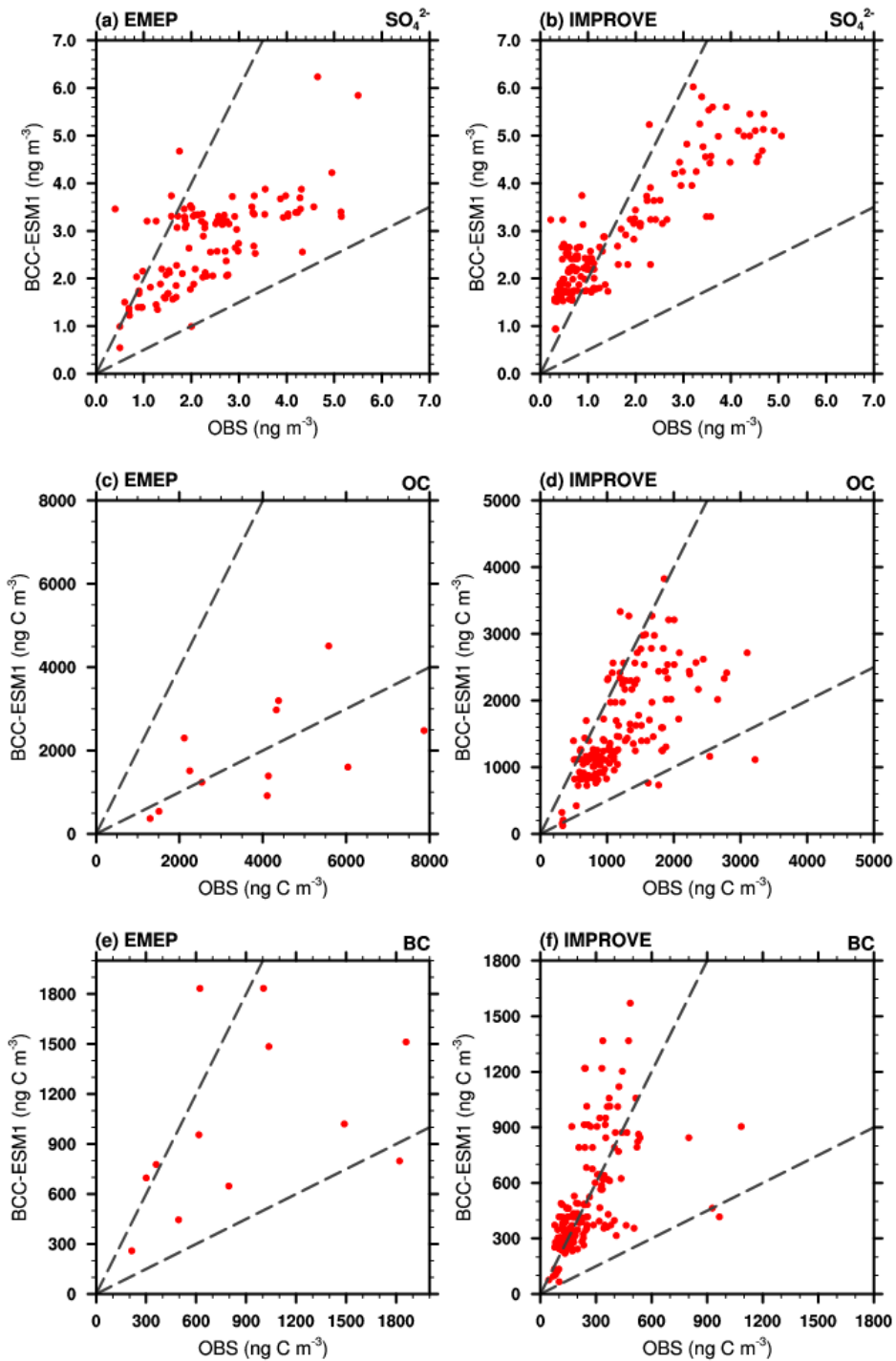
Figure 15. Scatter plots showing observed versus simulated multi-years averaged annual mean sulfate (SO_4^{2-}), organic carbon (OC), black carbon (BC) mixing ratios at IMPROVE and EMEP network sites. Observations are averages over the available years 1990–2005 for IMPROVE sites, and 1995–2005 for EMEP sites. Simulated values are those at the lowest layer of BCC-ESM1.

Table 7. Observed versus simulated concentrations of sulfate (SO_4^{2-}), organic carbon (OC), black carbon (BC) for the regional mean and spatial standard deviation, minimum and maximum values at HIPPO aircraft observations (BC only), IMPROVE and EMEP network sites, and the spatial correlation between observed and simulated multi-years averaged annual means. Simulated values are selected for the same locations and same valid observation time. The data used same as those in Figure 12.

	EMEP			IMPROVE			HIPPO
	$SO4^{2-}$ **(Obs/Model)**	**OC** **(OBS/Model)**	**BC** **(OBS/Model)**	**$SO4^{2-}$** **(OBS/Model)**	**OC** **(OBS/Model)**	**BC** **(OBS/Model)**	**BC** **(OBS/Model)**
Mean Values	2.37/2.74	3844/1919	884/1022	1.53/2.79	1215/1565	249/504	8.2/11.1
Std Deviation	1.16/0.93	1997/1215	572/526	1.30/1.20	572/745	164/296	27.9/21.0
Min Values	0.40/0.55	1296/369	214/259	0.22/0.94	322/123	45/66	0.0025/0.066
Max Values	5.50/6.24	7867/4510	1859/1834	5.07/6.02	3219/3827	1084/1570	558.91/267.11
Correlation **(Obs and Model)**	0.67	0.56	0.40	0.90	0.63	0.55	0.51
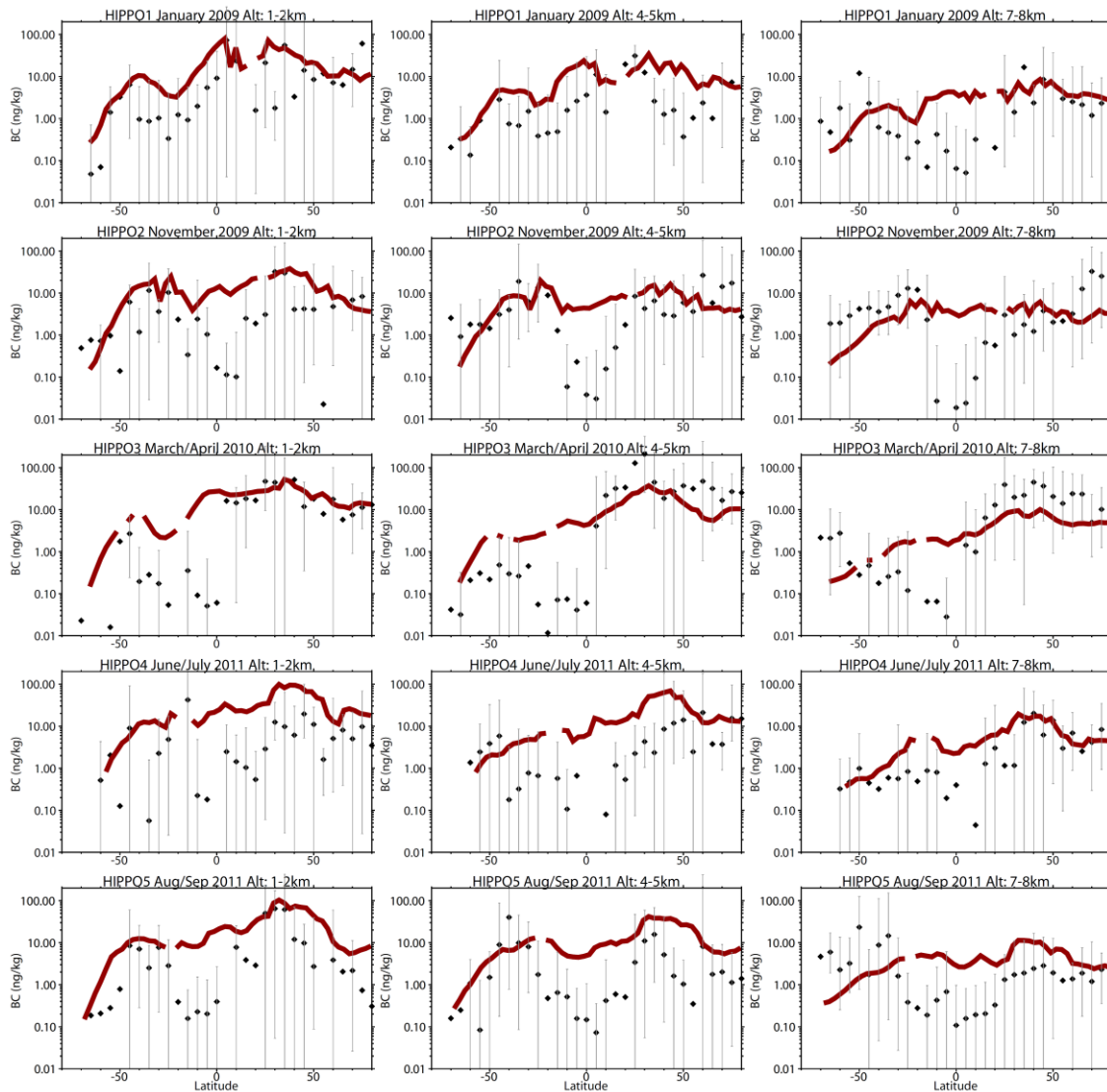
Figure 16. Comparison of modelled black carbon (BC) aerosol (red lines) with observations from HIPPO aircraft campaigns over the Pacific Ocean (black symbols, bars represent the full data range). Observations from different HIPPO campaigns were averaged over 5 °latitude bins and three different altitude bands (left column: 1-2 km, middle column: 4-5 km, and right column: 7-8 km) along the flight track over the Pacific Ocean. Model results were sampled along the flight track and then averaged over the abovementioned regions for comparison.
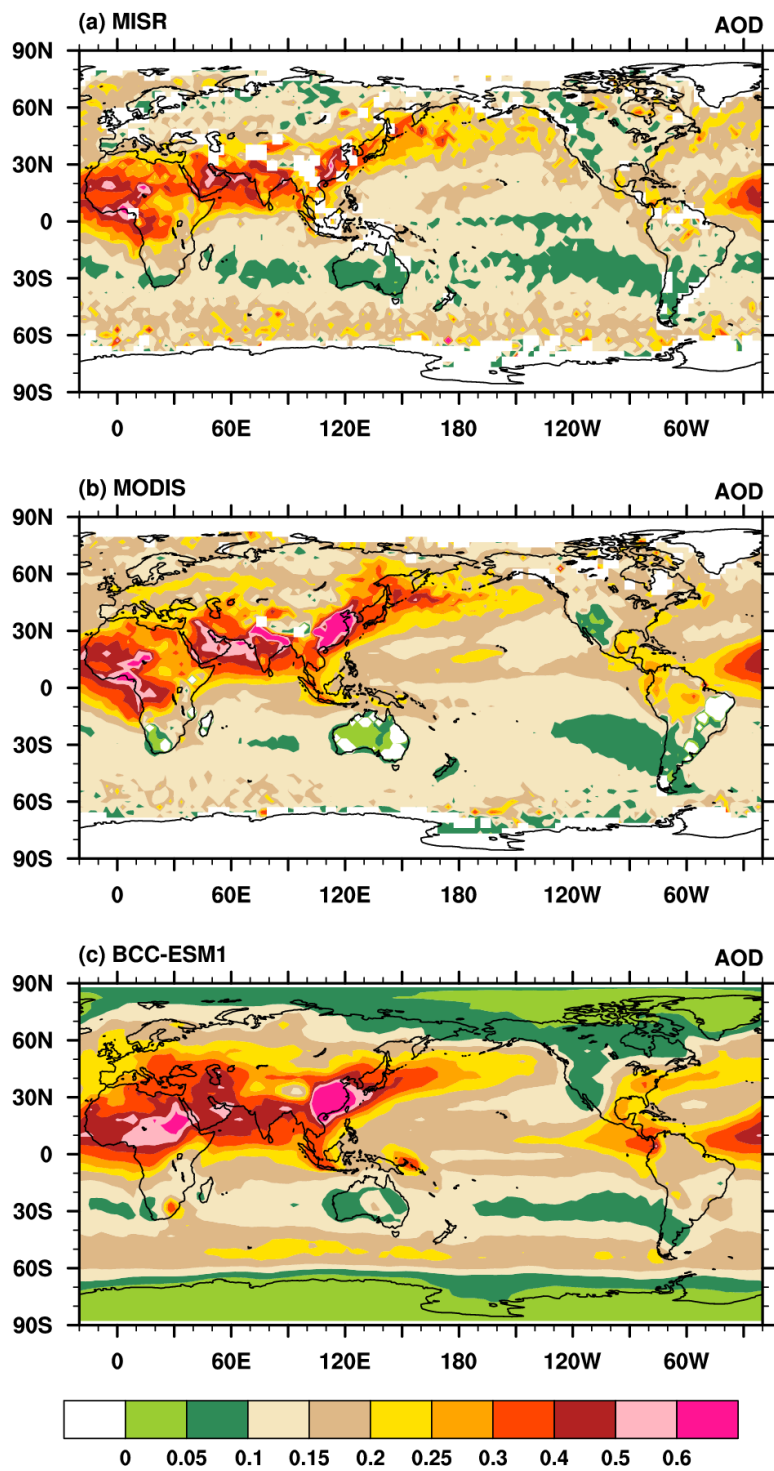
Figure 17. Global distribution of annual mean AOD simulated in BCC-ESM1 compared with the MISR and MODIS data for the year 2008.
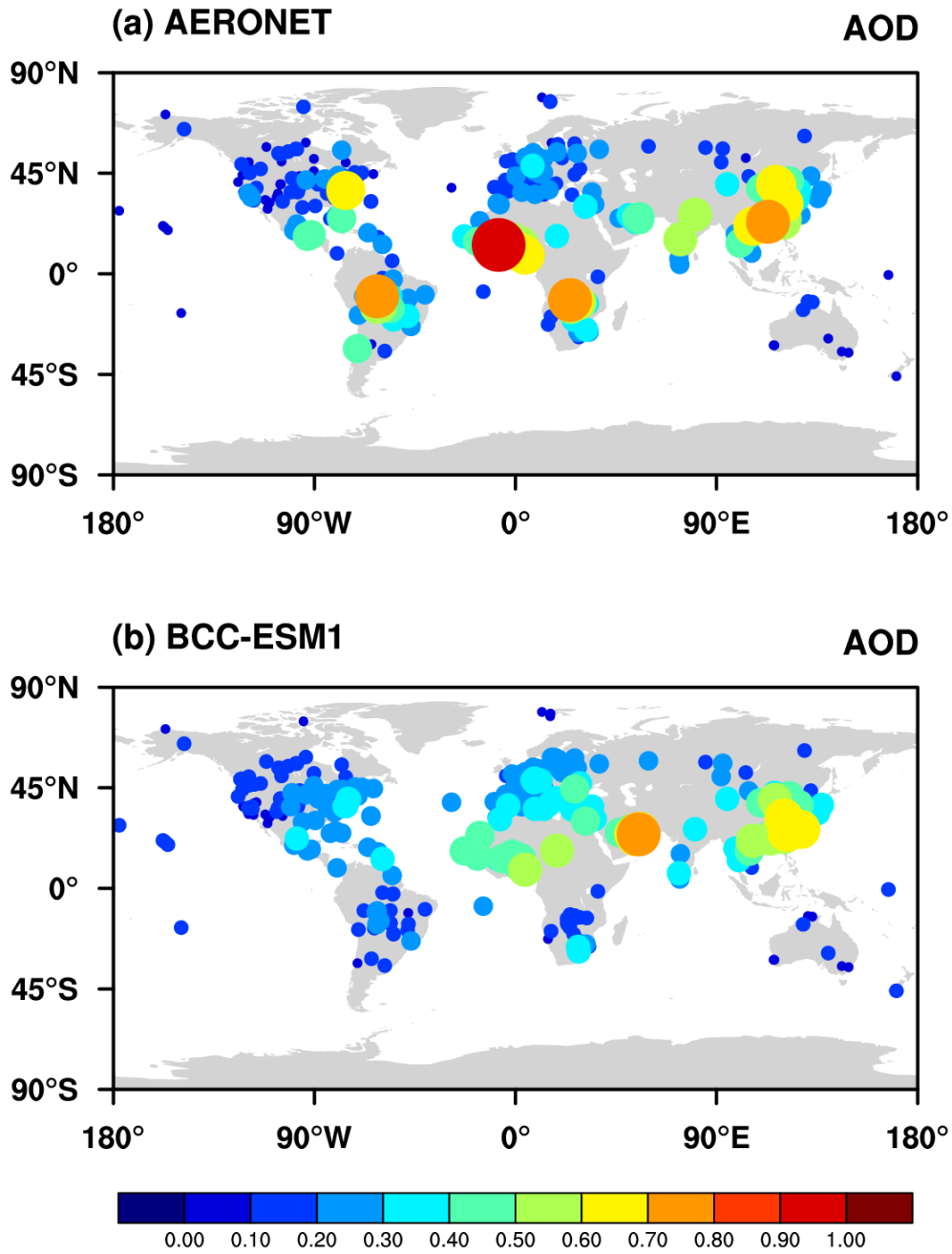
Figure 18. Observed versus simulated annual means of AOD at AERONET sites. Each data point represents the mean averaged for available monthly values of AOD. The dot sizes denote the magnitudes of AOD at sites. The spatial correlation is 0.56.
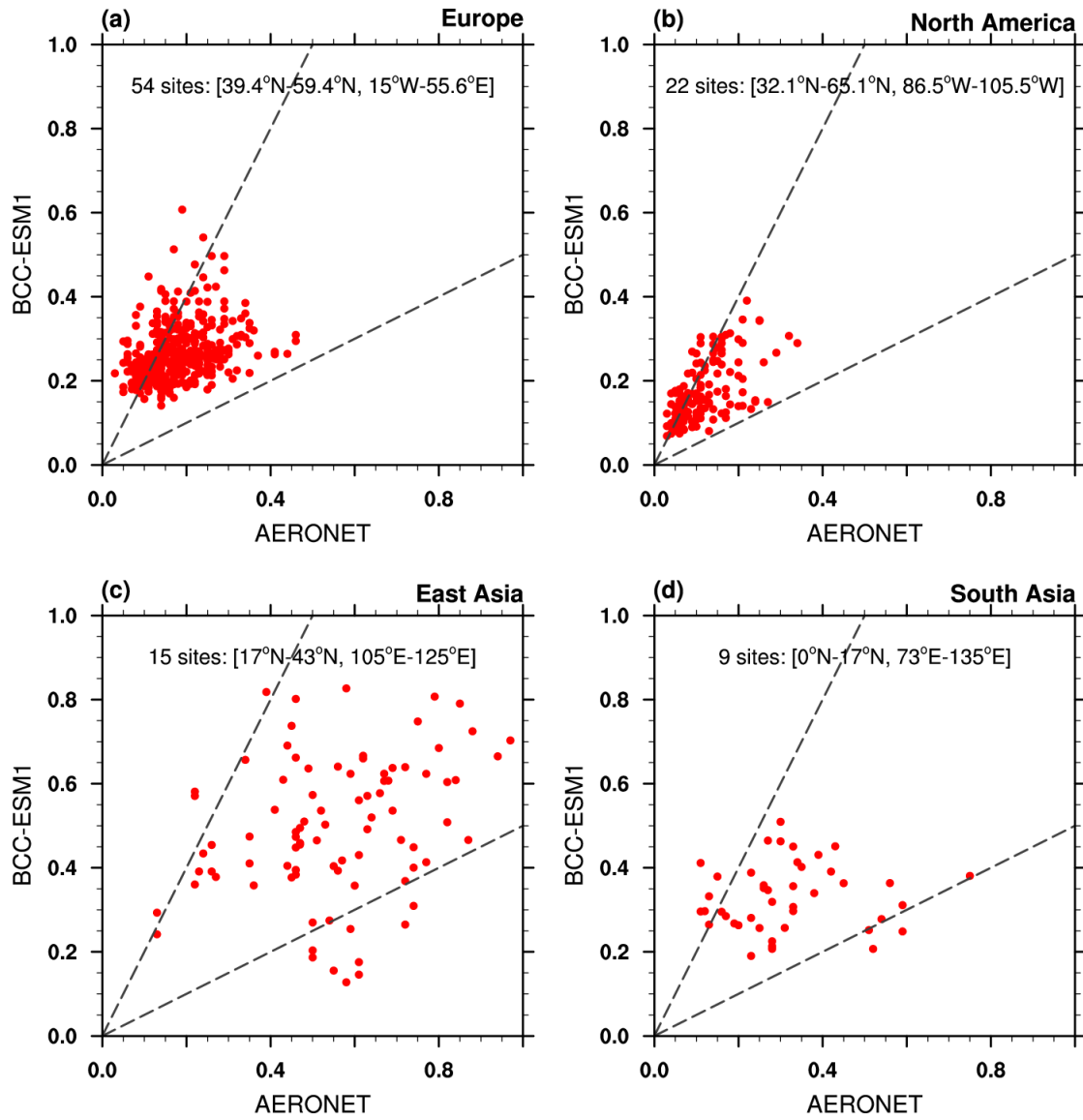
Figure 19. Scatter plots of observed versus simulated monthly mean AOD at AERONET sites in Europe, North America, East Asia, and South Asia over the period of 1998-2005.